

Peer review status:

This is a non-peer-reviewed preprint submitted to EarthArXiv.

1	For	eshock Behaviors and Mainshock Rupture Properties Associated with	
2		the 2025 Mw 8.8 Kamchatka Earthquake Sequence	
3			
4	This preprint was submitted to Earthquake Research Advances for peer review on 11/22/2025		
5			
6	Phuc Mach¹ (pmach3@gatech.edu), Xu Si¹ (xsi33@gatech.edu), Dun Wang²		
7	(wang	dun@cug.edu.cn), Robert Shcherbakov³ (rshcherb@uwo.ca), Ping He² (phe@cug.edu.cn),	
8	Tuncay Taymaz <sup>4,5</sup> (taymaz@itu.edu.tr), Chang Ding1 (cding64@gatech.edu), Zhigang Peng <sup>1</sup>		
9	(zpeng	g@gatech.edu)	
10	1.	School of Earth and Atmospheric Sciences, Georgia Institute of Technology, Atlanta,	
11		United States, 30332	
12	2.	Chinese University of Geosciences, Wuhan, Hubei, China, 430074	
13	3.	Department of Earth Sciences, Western University, London, Ontario, Canada 54901	
14	4.	Department of Geophysical Engineering, İstanbul Technical University, ITU Ayazaga	
15		Campus, Maslak TR-34469, Sarıyer, İstanbul, Türkiye	
16	5.	Disaster Management Institute, İstanbul Technical University, ITU Ayazaga Campus,	
17		Maslak TR-34469, Sarıyer, İstanbul, Türkiye	

Abstract The July 29 2025 Mw 8.8 Kamchatka earthquake ruptured the plate interface off the east coast of the Kamchatka Peninsula along the Kuril-Kamchatka subduction zone. Following the mainshock, tsunamis were recorded in multiple countries along the Pacific Ocean boundary and its islands, along with the eruption of several volcanoes in Kamchatka. The mainshock was preceded by a strong foreshock sequence that began with a Mw 7.4 event on July 20, located near the mainshock hypocenter. However, the physical mechanisms driving this foreshock sequence is not completely clear. Here, we present a detailed seismological and geodetic analysis of the sequence, combining teleseismic back projection, a single-station template matching detection for foreshocks and aftershocks, a statistical analysis of the entire sequence, and the GNSS and InSAR data for aseismic deformation. We find that the mainshock ruptured predominantly to the southwest direction with a total source duration of ~220 s. The M7.4 foreshock sequence triggered afterslip along the plate interface, which likely drove an expanding aftershock of its own and eventually triggered the mainshock nucleation. The aftershock productivity of the M7.4 event is also several times higher than several M7+ events before and after the M8.8 mainshock, which increases the probability of triggering a larger mainshock. We also find possible segmentation of the megathrust rupture zone along the Kuril-Kamchatka subduction zone that is separated by higher topography in the upper plate. The integrated approach provides an improved understanding of the physical mechanisms of foreshocks and segmentation of mainshock ruptures along major subduction zones, which is directly relevant to short-term forecasting and seismic hazard assessment of megathrust earthquakes in this and other regions.

19

20

21

22

23

24

25

26

27

28

29

30

31

32

33

34

35

36

37

38

39

# 41 Major points:

- 1. The 2025 M8.8 Kamchatka mainshock featured a predominant southwestward rupture of ~500 km along the subducting plate interface.
- Afterslip following the 2025 M7.4 foreshock drives its aftershock migration and likely
   triggers the M8.8 mainshock.
- 3. A possible soft barrier near Cape Shipunskiy likely separates the 2025 mainshock and
   other recent earthquake ruptures.

# 48 **Keywords**:

50

49 Kamchatka, foreshock, aftershock, back projection, afterslip, megathrust earthquake

#### 1. Introduction

On July 29, 2025, at 23:24:52 UTC, a moment magnitude (Mw) 8.8 earthquake occurred off the east coast of the Kamchatka Peninsula (Figure 1). The event occurred in the Kuril-Kamchatka subduction zone, one of the most seismically active plate boundaries around the Pacific Rim. This plate interface has hosted multiple large interplate earthquakes during the past century, including a Mw 8.8-9.0 event on November 4, 1952 (Johnson and Satake, 1999; MacInnes et al., 2010; Bilek and Lay, 2018). The 2025 Mw 8.8 mainshock ruptured a similar patch and was preceded by a foreshock sequence that started on July 20, with the latest event being a Mw 7.4 event (Bradley and Hubbard, 2025a; Hubbard and Bradley, 2025a; Stein et al., 2025). The foreshock event occurred close to the mainshock hypocenter, and its productivity appeared to be higher than other Mw 7+ events that occurred before and after the Mw 8.8 mainshock (Stein et al., 2025).

It is worth noting that a smaller Mw 7.0 earthquake occurred near the hypocenter of the Mw 7.4 event on August 17 2024 but was not followed by a larger event (Bradley and Hubbard, 2024; Chebrov et al., 2025). This highlights the difficulty of using elevated seismicity alone (i.e., foreshocks) as a harbinger for larger earthquakes (Peng and Lei, 2025). In other regions such as the Japan Trench and northern Chile, recent studies showed elevated foreshock rates, migrating seismicity, and short-term slow slip before some large events (Kato et al., 2012; Ruiz et al., 2014), whereas other large earthquakes show little or no clear pre-seismic deformation or precursory signals (Roeloffs, 2006; Peng and Lei, 2025).

With high-resolution earthquake catalogs and geodetic observations, there is a renewed interest in studying foreshock activity and short-term aseismic transients relating to the nucleation of the mainshock around the world (Beroza et al., 2021; Zhou et al., 2022; Wang et al., 2024, 2025; Bletery and Nocquet, 2023, 2025; Bradley and Hubbard, 2024; Martínez-Garzón and Poli, 2024; Peng and Lei, 2025; Lippiello et al., 2025; Rodkin et al., 2025; Goltz, 2025). In this study, we assemble a unified seismological and geodetic dataset of the 2025 Kamchatka sequence to characterize its pre-seismic evolution and co-seismic rupture. We integrate the teleseismic back projection of P waves to image the mainshock ruptures, and a single-station template-matching detection to enrich the catalogs of foreshocks and the earliest

aftershocks. Using these tools, we quantify the statistical behavior before and after the mainshock, map the timing and migration of high-frequency radiation during the mainshock rupture, and delineate the geometry, segmentation, and depth extent of the mainshock slip on the plate interface. We complement the seismic analysis with available InSAR images and GNSS recordings to place constraints on the onshore displacement, possibly aseismic transients before the mainshock, and to track the onset of early post-seismic deformation. We also examine potential segmentations of megathrust ruptures in the study region.

# 2. Tectonic Background and the Initial Observations of the M8.8 Mainshock

The Kamchatka Peninsula is at the northern section of the 2100-km Kuril-Kamchatka arc (Figure 1), where the Pacific plate subducts beneath the Okhotsk microplate. This subduction has produced the island chain along the arc, a continuous volcanic front, and the deep Kuril-Kamchatka Trench (Ruppert et al., 2007). The plate convergence near the 2025 mainshock rupture is rapid and directed to the northwest, with rates estimated to be 80 mm/yr (DeMets, 2010). This arc shows a variety in obliquity with the deformation south of the Kamchatka peninsula partitioned into thrust motion on the megathrust and strike slip in the forearc, while the north toward Kamchatka becomes more trench normal. The Wadati-Benioff zone is well defined, and the slab dip shallows under the influence of the Meiji Seamount chain and the Aleutian transform (Hayes et al., 2018).

The earthquake productivity in this region is among the highest worldwide, with megathrust earthquakes occurring near the trench down to the depths of 40-60 km, and intermediate-depth to deep-focus earthquakes up to 600-700 km in the Sea of Okhotsk (Zhan et al., 2014). Historic aftershock zones of large events have been used to infer segmented behavior and to define seismic gaps. For example, the central Kuril sequence started with an Mw 8.3 earthquake in November 2006 that ruptured a long-standing gap, followed by an Mw 8.1 outer rise normal faulting event in January 2007 (Ammon et al., 2008), forming a notable doublet. The 2025 event took place in a region that was also ruptured during the 1952 M8.8-9.0 event, which had a devastating tsunami impact (Johnson and Satake, 1999; MacInnes et al., 2010). However, finite-fault slip inversions from teleseismic and geodetic observations show

that the ruptures of the 1952 and 2025 events appear to complement each other (Mikhailov et al., 2025; Yagi et al., 2025).

With this magnitude, the 2025 event is categorized as one of the ten largest earthquakes worldwide since 1900 (Bradley and Hubbard, 2025a). Based on finite-fault slip inversions, the mainshock slip-plane size was estimated to be 600 km along strike in length, by 140-175 km in width, orthogonal to dip (USGS; Bradley and Hubbard, 2025a; Hubbard and Bradley, 2025b). The peak slip exceeded 9m across a broad region of the mainshock rupture zone (Yagi et al., 2025), and the total source duration was about 220 s (Xu et al., 2025). The location and the focal mechanism of the mainshock are consistent with reverse faulting on the subduction interface of the Kuril-Kamchatka arc.

The 2025 earthquake generated a Pacific-wide tsunami recorded by tide gauges and deep ocean sensors, but coastal impacts were uneven. In the Northern Kuril Islands, the maximum run-up was recorded up to 19 meters (Stein et al., 2025). The Pacific Tsunami Warning Center (PTWC) observed the amplitudes of 1.74 meters at Maui, Hawaii, and 1.13 meters in Crescent City, California, USA. However, despite the earthquake's large magnitude and the basin-wide propagation, there are not many local or distant impacts from the tsunamis. Additionally, records indicate that multiple Kamchatka volcanoes were activated in the days following the mainshock, including Mount Klyuchevskoy and Mount Krasheninnikov. Mount Klyuchevskoy had its continuing and intensive eruption with lava fountains starting July 30, just hours after the mainshock, with the long ash plumes documented through mid-August (Smithsonian Global Volcanism). Mount Krasheninnikov had its first eruption on August 2 after centuries of being inactive, with activity lasting about two weeks (FEB Russian Academy of Sciences, Smithsonian Global Volcanism). The temporal association between the Mw 8.8 mainshock and these eruptions is consistent with patterns discussed in prior work on earthquake-volcano interactions (Manga and Brodsky, 2006; Eggert and Walter, 2009).

As noted before, a Mw 7.0 reverse-faulting earthquake occurred east of Petropavlovsk-Kamchatsky on August 17, 2024 (Bradley and Hubbard, 2024; Chebrov et al., 2025). However, that sequence was not followed by another larger event. On July 20, 2025, a moment magnitude 7.4 event occurred farther east and initiated a distinct aftershock sequence whose

activity decayed with time until the 2025 moment magnitude 8.8 mainshock, which nucleated in the southwest of the 7.4 event (Stein et al., 2025). Two large aftershocks then occurred in the northern part of the aftershock region, including a Mw 7.4 on September 13, followed by a magnitude 7.8 on September 19 (Figure 1b). However, these aftershocks occurred in the north of the Mw 8.8 mainshock, near the 1923 M8.5 and 1959 M8.2 earthquakes (Hubbard and Bradley, 2025b; Bradley and Hubbard, 2025c). These significant events took place near each other along the Kuril-Kamchatka subduction zone just outside of Cape Shipunskiy (Figure 1a).

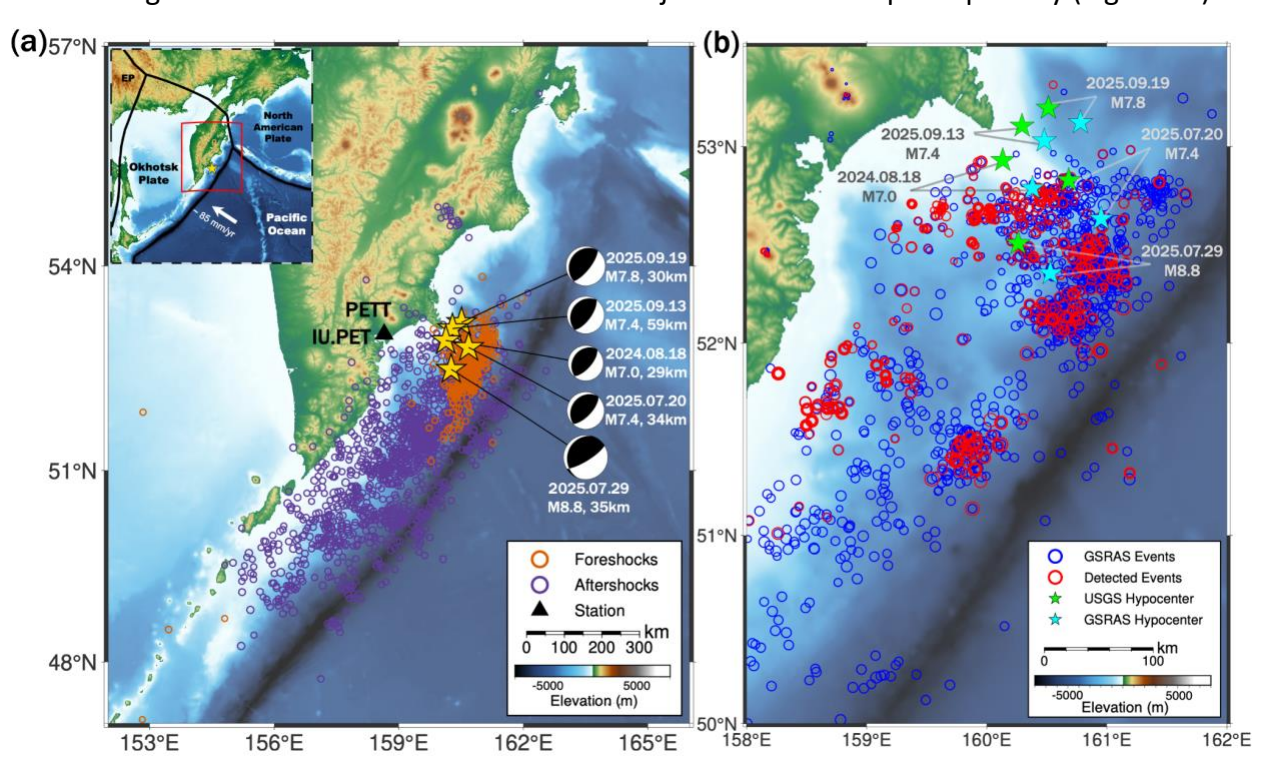
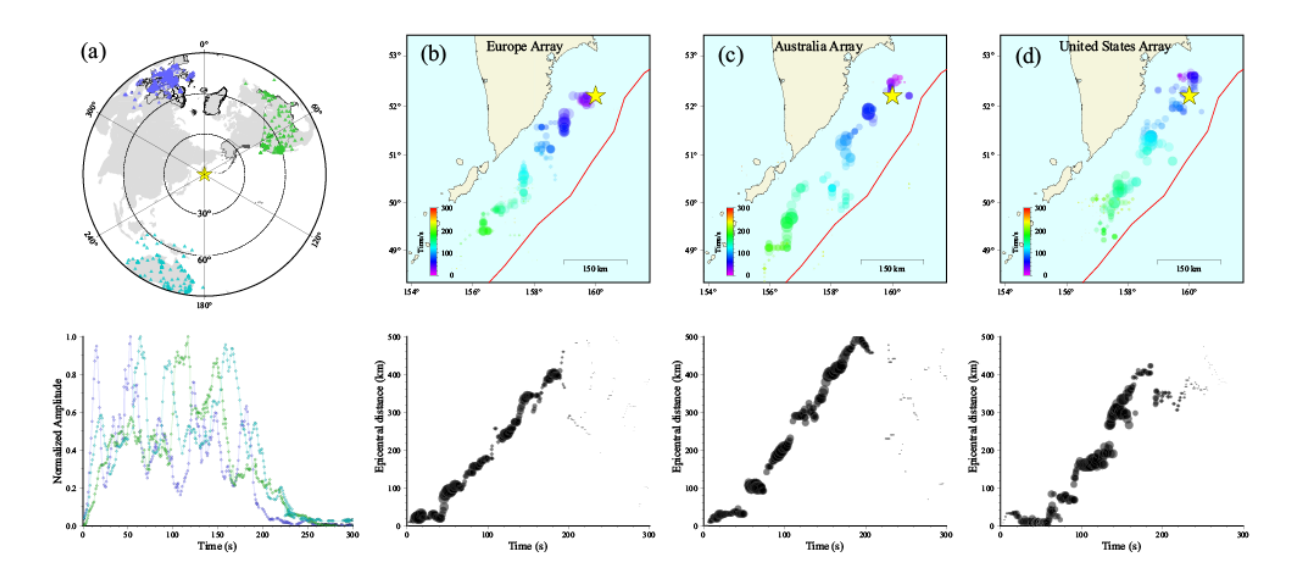


Figure 1. (a) Map view of the M8.8 Kamchatka earthquake with 10 days of foreshocks (orange), 10 days of aftershocks (purple) and focal mechanism (with magnitude and depth) of the Mw≥7.0 events. (b) Map view of the local catalog events (blue) from the Geophysical Survey of the Russian Academy of Sciences (GSRAS) and template-matching detected events (red) with the location of the Mw≥7.0 events in USGS and GSRAS catalogs.

#### 3. Mainshock Rupture Properties from a Back-projection Analysis

We first apply a P-wave back-projection method (Wang et al., 2011; Wang et al., 2016; Kiser and Ishii, 2017) to image the rupture process of the 2025 Kamchatka Peninsula earthquake using teleseismic data recorded by regional arrays in Europe (EU), the United States

(US), and Australia (AU) (Figure 2a). The same procedure has been applied to image the rupture extent following the 2024 M7.5 Noto Peninsula, Japan earthquake (Peng et al., 2025a) and the 2025 M7.7 Sagaing fault earthquake in Myanmar (Peng et al., 2025b). As was done before, the locations of the maximum energy points are plotted to highlight the primary rupture features (Figure 2). These three arrays (EU, AU, and US) are located to the northwest, southwest, and northeast of the epicenter, respectively, with epicentral distances ranging from 30° to 90°, which is the optimal range for teleseismic P-wave back-projection (Kiser and Ishii, 2017). While the results from these arrays differ slightly, their primary features are mutually consistent: the mainshock ruptured predominantly southwestward along the subduction interface with a rupture length of approximately 500 km. The total source duration is about 220 s, consistent with the finite-fault inversion results (Xu et al., 2025), and the average rupture speed is ~2.3 km/s. However, the mainshock source functions likely contained 3-4 sub-events, and the rupture speeds were not uniform, indicating multiple peaks of high frequency energy radiations during the mainshock.



**Figure 2.** Teleseismic P-wave back-projection of the 2025 Kamchatka Peninsula Fault earthquake. (a) (Top) Locations of the Europe (EU), Australia (AU) and United States (US) regional seismic arrays. (Bottom) The normalized amplitudes as a function of time for three arrays. (b) Top: spatial distribution, timing, and amplitude of maximum-correlation back-projection using the EU array for the 2025 Kamchatka Peninsula Fault earthquake. Bottom:

time—distance plot showing the rupture propagation speed of the maximum energy point over time. The yellow star indicates the mainshock epicenter. (c) and (d) Same as (b), but using the AU and US arrays, respectively.

### 4. InSAR Data Analysis

To capture the coseismic deformation field, we analyze three Sentinel-1A/C interferogram pairs: one descending pair (track 060, 19–31 July 2025) and two ascending pairs (track 111, 23 July–4 August 2025; track 038, 18–30 July 2025). Standard interferometric processing steps ensured precise image alignment and reliable phase retrieval, after which the interferograms were geocoded into the UTM projection. Atmospheric delays were corrected using GACOS products (Yu et al., 2018), which proved particularly effective in volcanic regions where steep relief commonly amplifies tropospheric phase distortions.

The unwrapping interferograms (Figure 3) reveal pronounced coseismic deformation across the onshore Kamchatka region, despite the earthquake occurring offshore more than 100 km far from the nearest coastline. Retrieved line-of-sight (LOS) displacements range from –22.7 to 91.9 cm for descending track 060, from –108.4 to 18.3 cm for ascending track 111, and from –28.8 to 13.6 cm for ascending track 038 (Figure 3a–c). The deformation field is characterized by opposite LOS polarities between ascending and descending geometries, a broad spatial extent exceeding 400 km, and a smooth gradient (Figure 3d). These features indicate that the rupture was dominated by a moderate horizontal component accompanied by substantial vertical uplift. Such a wide and gentle deformation pattern is diagnostic of slip on a shallowly dipping offshore megathrust fault.

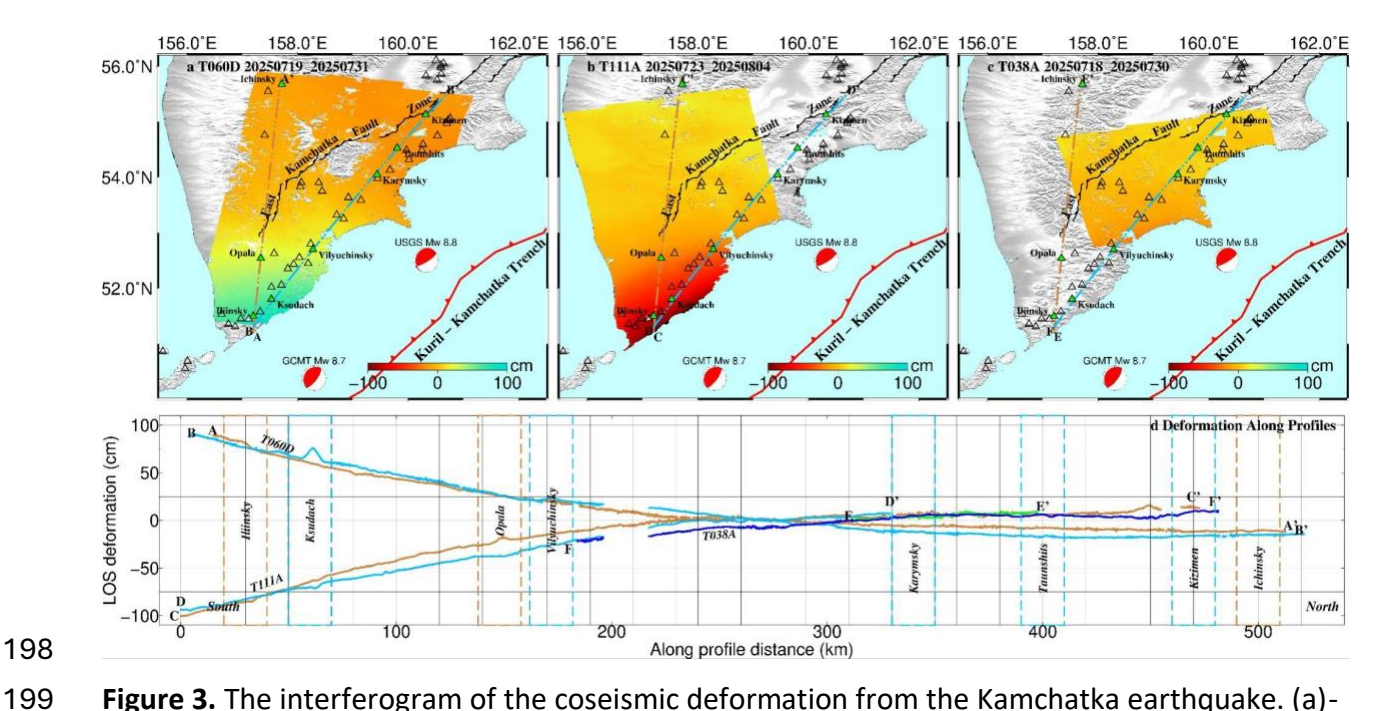


**Figure 3.** The interferogram of the coseismic deformation from the Kamchatka earthquake. (a)-(c) Retrieved line-of-sight for three different tracks. (d) LOS deformation field in comparison to the along-profile distance.

As noted before, the mainshock was reported to have triggered activity at seven Holocene volcanoes, including a strong eruption of Krasheninnikov (GVP, 2025). Because the eruption of Krasheninnikov occurred several days after the mainshock, it falls outside the temporal coverage of the InSAR pairs analyzed in this study. Moreover, no clear volcanic activity—related deformation signals are detected at the other six volcanoes. In contrast, subtle deformation features are suggested at Ksudach and Opala (Figure 3d). Overall, these findings underscore the heterogeneous nature of earthquake—volcano interactions, with only certain volcanic systems responding measurably to large subduction earthquakes (Walter & Amelung, 2007; Eggert & Walter, 2009).

## 5. Foreshock and Aftershock Patterns from Local and Template Matching Catalogs

In this section, we analyze the microseismicity before and after the mainshock from both local and global earthquake catalogs and a template-matching-based catalog. Due to the offshore source geometry and data access, continuous recordings from a single nearby broadband station IU.PET was available. A high-resolution earthquake catalog was therefore

constructed by applying a single-station template matching to the continuous data. Matched-filtered detection uses waveform similarity to recover small earthquakes that original catalogs miss, which lowers the magnitude of completeness and sharpens clustering in space and time (Gibbons and Ringdal, 2006; Peng and Zhao, 2009; Yang et al., 2009; Ross et al., 2019). With this method, we enhance our observation of spatio-temporal evolutions of the July 20 foreshock sequence and events right after the Mw 8.8 mainshock.

Using the catalogs from the United States Geological Survey (USGS) and the local seismic network called the Geophysical Survey of the Russian Academy of Sciences (GSRAS), a single station template matching detector was applied to recover events that were poorly recorded or absent from the original catalogs. Firstly, we extract all events recorded by station IU.PET from the local catalog, obtaining a total of 9,143 events spanning August 1, 2024, to September 22, 2025. Each event is then processed using EQTransformer for automatic phase picking, with thresholds of P\_threshold = 0.1 and S\_threshold = 0.1. We retain only those events that contained both P and S arrivals within the same record, resulting in 3,441 qualified events. Subsequently, we apply a 1−10 Hz band-pass filter to both the continuous and template waveforms at IU.PET. For each waveform, we extract a time window extending 5 s before the P-wave arrival and 8 s after the phase arrivals. Finally, we compute the mean cross-correlation coefficients (CCCs) between the template and continuous waveforms, and considered detections with CCC ≥ 0.7 as valid new events.

In total, 523 templates produced successful detections, resulting in 999 new events with mean correlation coefficients (cc)  $\geq$  0.7 during a 78-day period from 6 July to 22 September 2025 surrounding the M8.8 mainshock. A relatively high correlation threshold was chosen, rather than a conventional median absolute deviation (MAD) criterion, to ensure the reliability of the newly detected events. Since only a single continuous station (IU.PET) was available, the detected events were assigned the hypocenters of their corresponding templates, meaning their mapped locations coincide with those templates rather than being independently relocated. The magnitudes of the detected events were estimated based on their relative amplitudes with respect to the templates. Immediately after the mainshock, early aftershocks are recovered with a match-filtered technique while still embedded in the coda. Figure 4 shows an example of a

detected early aftershock event using the matched-filter technique. The newly detected event occurred at 27100s (~7.5 hours) following the mainshock and had an inferred magnitude of 3.9.

Figure 1b shows GSRAS locations for the ten days of aftershocks following the M 8.8 mainshock, with template-matched detections overlaid. Because only one continuous station is available, detections were assigned the hypocenter of their used templates; thus, the mapped locations of detected events are colocated with the templates rather than independently relocated. A systematic catalog offset is also evident, in which for events of magnitude 7.0 and larger, USGS epicenters plot consistently to the northwest of the corresponding GSRAS solutions (Figure 1b). This difference likely reflects distinct networks or velocity models and is noted when interpreting spatial patterns. Our conclusions are based on relative distributions within each catalog rather than on absolute epicentral agreement.

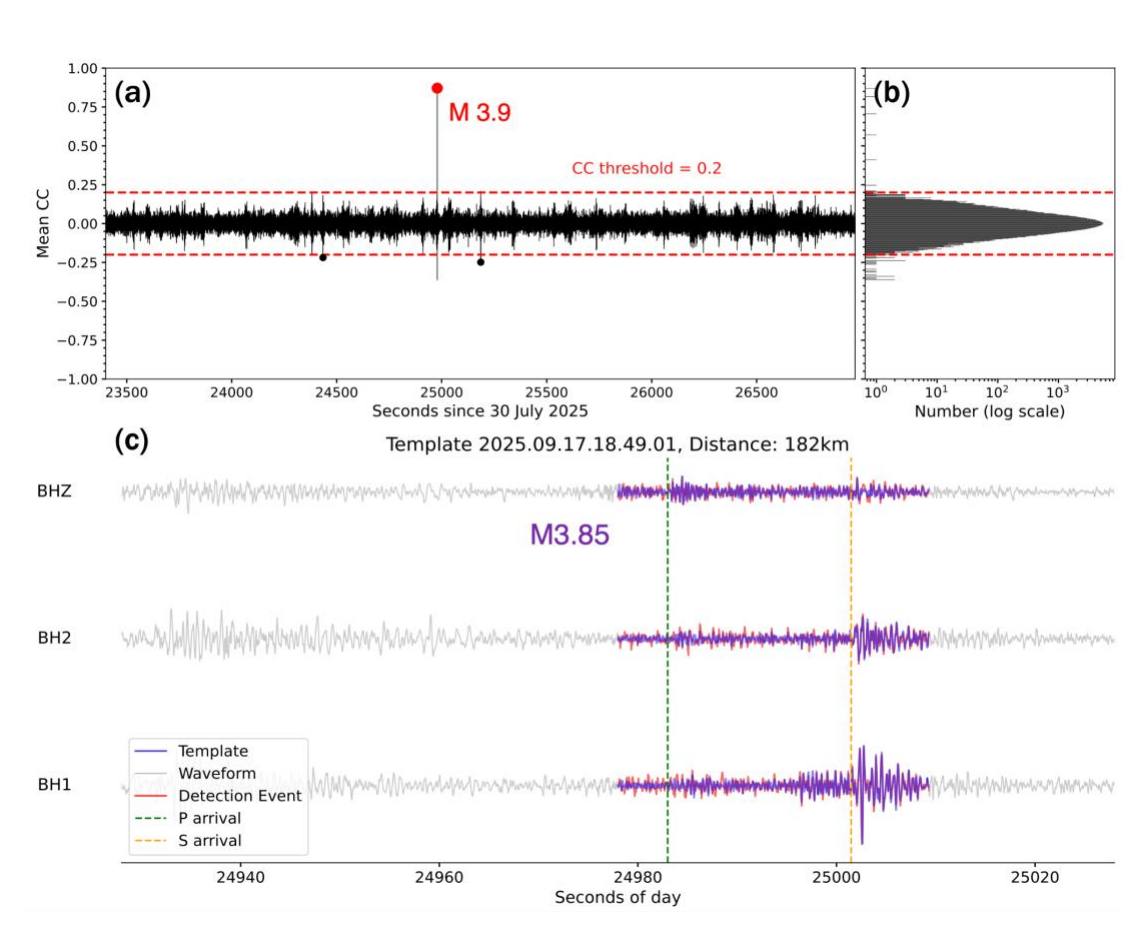


**Figure 4**. Example of a detected early aftershock. (a) Mean cross-correlation (CC) functions for the template event 20250917184901. The black dots are detections exceeding the absolute

threshold (red dashed line), and the red dot corresponds to the detected M 3.90 event matched with the M 3.85 template. (b) The histogram of the mean correlation coefficient functions. (c) A comparison of the template waveforms (red) and the continuous waveforms (grey).

When events are viewed in trench parallel coordinates along the Kamchatka-Kuril plate interface (Figure 5), foreshock activity beginning around the Mw 7.4 event is found to concentrate near the Mw 8.8 mainshock hypocentral region, with additional clusters distributed along the plate interface. In the first 20 hours after the Mw 7.4 event, detection events are concentrated in both northern and southern areas of the event, and the activity remains close to the hypocentral area. From July 21 to 28 2025, the foreshock distribution broadened mainly along strike toward the southwest while remaining confined in trench normal distance (Figure 5).

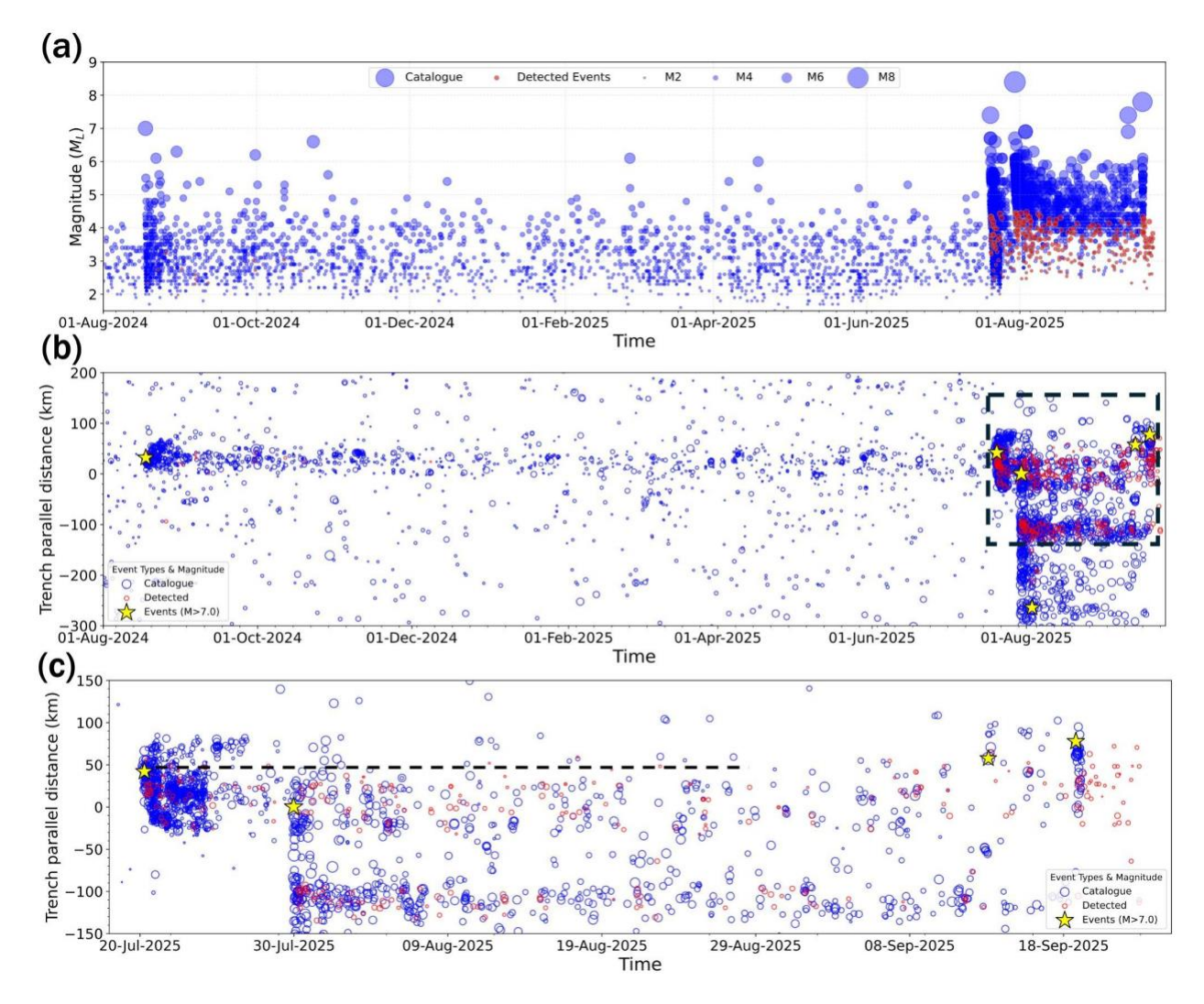


**Figure 5.** Observation of the Kamchatka sequence in the trench parallel distance. (a) The magnitude frequency distribution from 1 August 2024 to 25 September 2025. (b) Earthquake migration toward the rupture initiation point of the mainshock. Space-time diagram of all local catalogue events and detected events between 1 August 2024 and 23 September 2025, with earthquake origin locations indicated in terms of the distance along the trench axis (the width of the profile is 100 km). (c) Zoomed in on the smaller area of the sequence in figure b (black box). The aftershocks of the M8.8 event, starting from 20 August 2025 to 23 September 2025, included the M7.4 aftershock and M7.8 aftershock.

The aftershocks following the M7.4 foreshock appear to show systematic migrations aligned with the trench parallel direction (Figure 5c). To further quantify their migration patterns, we attempt to fit the seismicity front with two spatial migration functions: sqrt(t) for

fluid-driven seismicity (Shapiro et al., 1997; Sheng et al., 2022; Lei et al., 2024), and log10(t) for afterslip-driven seismicity (Peng and Zhao, 2009; Ross et al., 2017; Perfettini et al., 2018). Both fits capture a clear decelerating expansion of activity ( $R^2 \approx 0.67$  for Vt and  $R^2 \approx 0.80$  for  $log_{10}(t)$ ; Figure 6c–d), suggesting a systematic migration of seismicity with time. From Figure 6c-d, the rear events following the aftershock expansion are fitted as R = -0.09Vt + 19.68 or  $R = -29.64log_{10}(t) + 136.83$ . Although both curves are close to each other in shape, the log10(t) function fits the aftershock expansion at the southern front slightly better when compared to the sqrt(t) function. We also examine the spatial expansion for the M7.0 event in 2024, the M8.8 mainshock, and two M7+ aftershocks (Figure 5c). While a minor aftershock expansion is observed following the 2024 Mw 7.0 event, its spatial extent is limited. We also observe a minor expansion of aftershocks in the NE direction following the 2025 Mw 8.8 mainshock. However, most of them occurred within the region marked by the dashed line (Figure 3c), until the two Mw>7 events in September 2025.

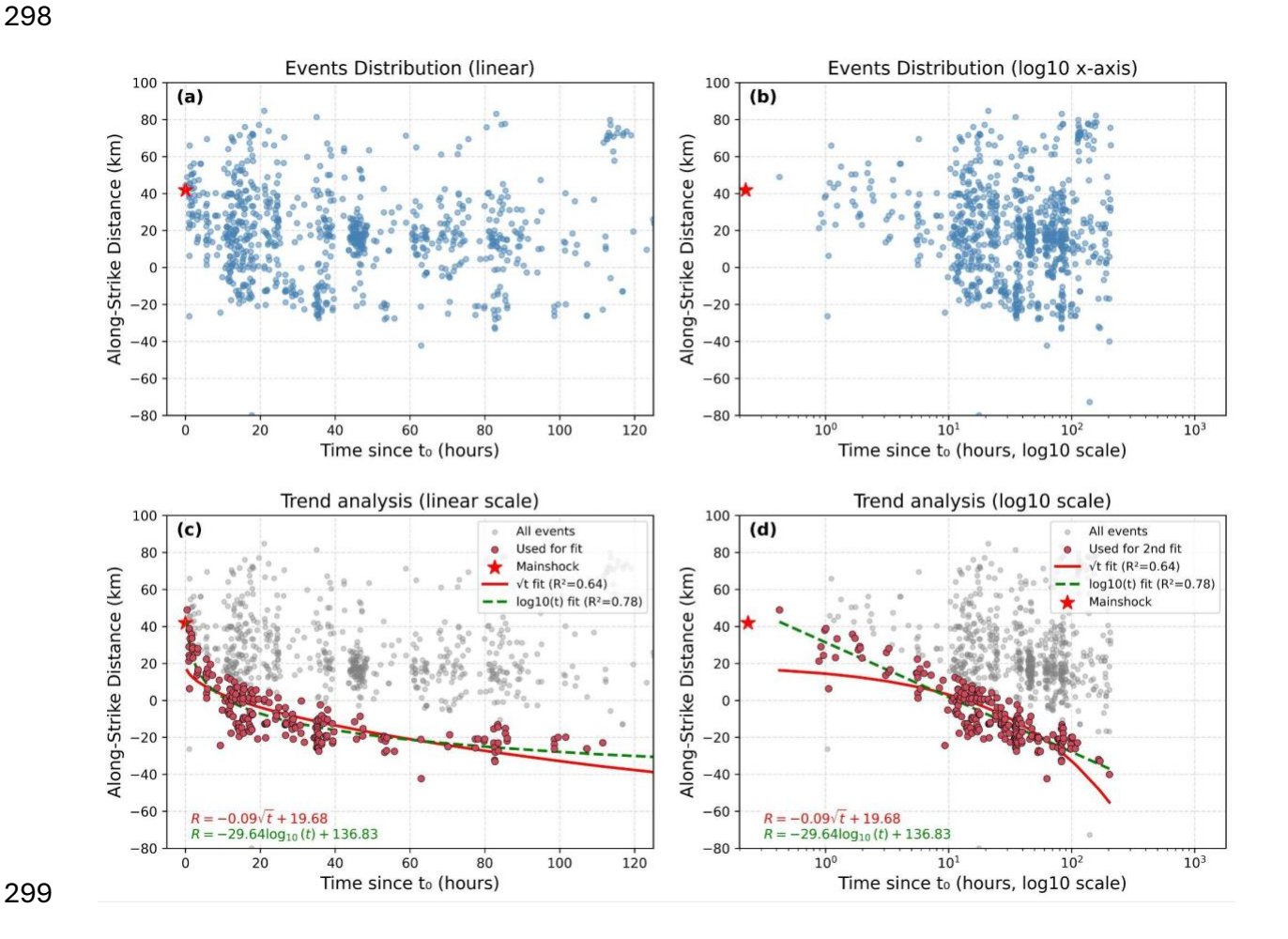


**Figure 6.** Spatiotemporal evolution of seismicity along the fault. Panels (a) and (b) show the distribution of events with time since the reference origin ( $t_0$ ) plotted on linear and logarithmic x-axes, respectively. Each dot represents an individual event, and the along-strike distance is measured relative to the mainshock location. Panels (c) and (d) present trend analyses for the same catalog, where the red points indicate the events used for fitting. Two empirical relationships are tested: the red solid line corresponds to a  $\forall t$  fit ( $R^2 = 0.67$ ), and the green dashed line corresponds to a  $\log_{10}(t)$  fit ( $R^2 = 0.80$ ).

Next, we examine the continuous five-minute-sampling GNSS recording at PETT. We first rotate the two horizontal components from north-south and east-west to trench parallel and normal components using a strike of 217 degrees from the M8.8 mainshock (Figure 7). The co-seismic offset for the Mw7.4 foreshock and the Mw8.8 mainshock is obvious. In the foreshock window after the 20 July Mw 7.4 event, the trench normal component shows a steady landward motion of a few centimeters that is well described by a simple logarithmic time fit,  $d = 36 + 12\log_{10}(1 + \frac{t}{1.71})$ . On the other hand, the other two components do not show any obvious co-seismic offset and post-seismic deformation (Figure 7b). Right after the 29 July mainshock, both trench normal and along strike components grow with a similar log-time form,  $d = 466 + 39\log_{10}(1 + \frac{t}{0.02})$  and  $d = 344 + 33\log_{10}(1 + \frac{t}{0.02})$  respectively, and reach several tens of centimeters by mid-August (Figure 7a). The onset of the trench normal motion closely tracks the rise in cumulative local aftershocks.

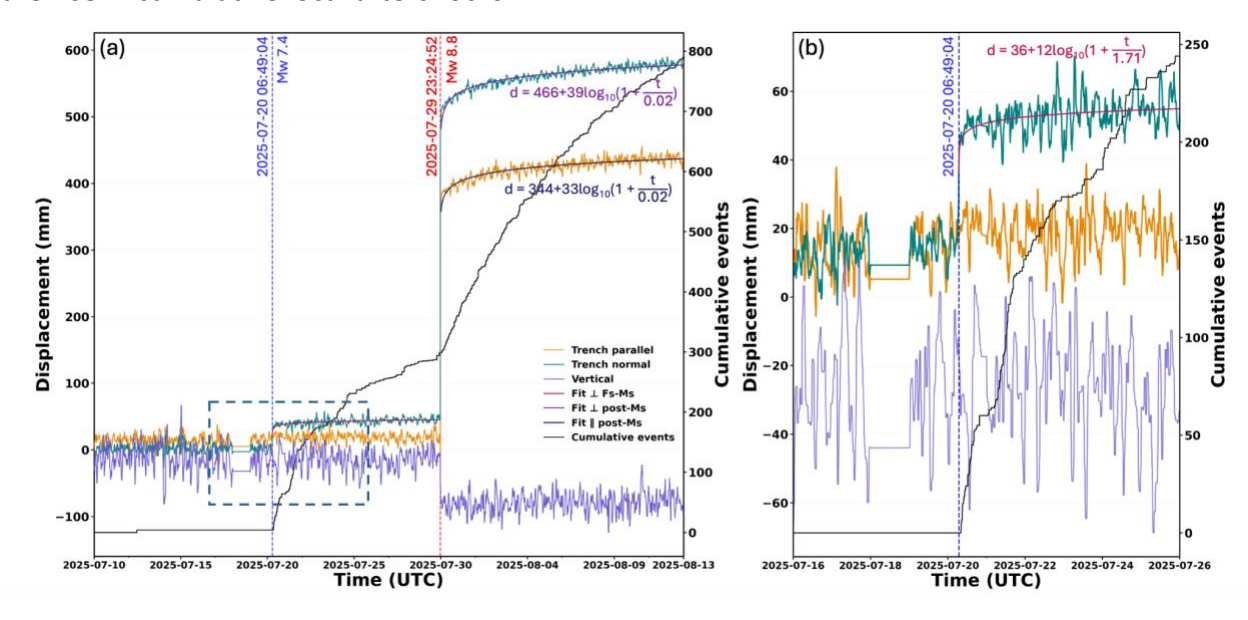


**Figure 7.** (a) GNSS station PETT data in trench parallel, trench normal, and vertical starting from 10 July 2025 to 13 August 2025 with curve fit. (b) Zoom in on the blue box time range in (a) between 16 July 2025 and 26 July 2025.

# 6. Statistical Analysis of Foreshock and Aftershock Sequence

In this section, we analyze the statistical aspects of the sequence, which include the mainshock, its strong foreshock sequence starting from July 20, 2025, and three significant aftershocks of the Mw 8.8 mainshock. Three analyzed aftershocks include a Mw 6.9 event that occurred 45 minutes after the mainshock, a Mw 6.8 that occurred on August 3, and a Mw 7.8 event that occurred on September 18. This is consistent with what is expected from Båth's law, which states that, on average, the magnitude difference between the mainshock and the largest aftershock is approximately 1.2 (Shcherbakov and Turcotte, 2004).

Because the local GSRAS catalog is likely not complete for aftershocks that are relatively far away from the Kamchatka Peninsula, the global earthquake catalog from the USGS is primarily used in this section. To model the sequence, we subdivide the seismic events according to three main time episodes. The first episode of the sequence constitutes events that occurred before the Mw 7.4 foreshock, starting from July 29, 2024, which can be treated as background seismicity. The second episode is characterized by the aftershocks of the Mw 7.4 event right before the occurrence of the Mw 8.8 mainshock, and the third episode comprises the main aftershock sequence.

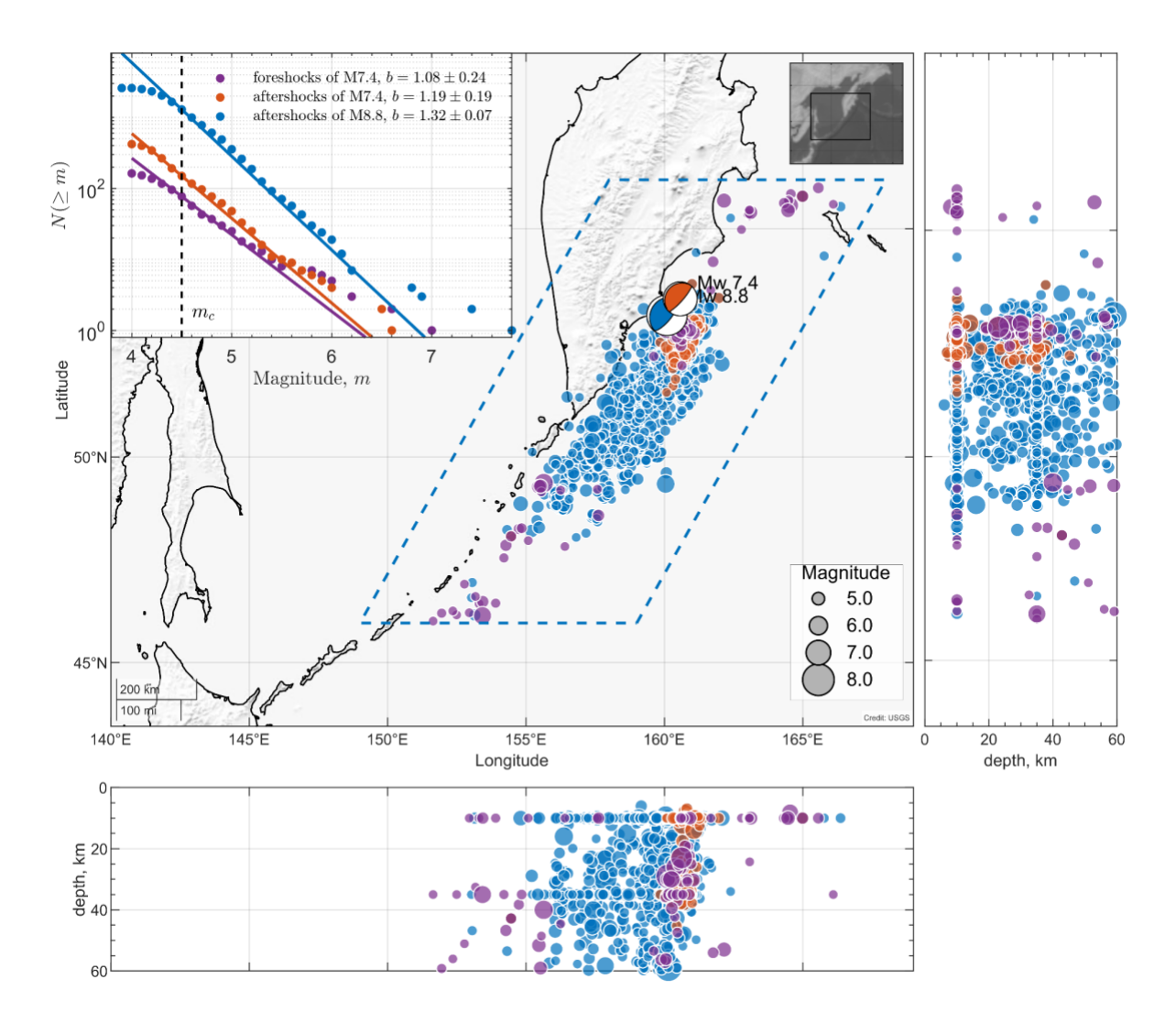


**Figure 8** Spatial distribution of events before and after the Mw 8.8 July 29, 2025, Kamchatka megathrust mainshock. Three episodes of the sequence are illustrated: the foreshocks of the Mw 7.4 event - purple sympols, the aftershocks of the Mw 7.4 event - orange symbols, and the aftershocks of the Mw 8.8 mainshock - blue symbols. The inset shows the frequency magnitude distribution of each episode of the sequence. Two panels on the right and bottom provide the depth distribution of the corresponding events.

The frequency-magnitude statistics of each episode of the sequence are plotted as an inset in Figure 8. To model the observed frequency magnitude statistics, we use the Gutenberg-Richter (GR) relation (Gutenberg and Richter, 1944): log10 (N) = log10

starting on 29 July 2024 and ending right before the Mw 7.4 event. For the second time range, we consider all events between the Mw 7.4 event and the Mw 8.8 mainshock and above magnitude 4.5. Similarly, the aftershocks of the Mw 8.8 event are used above magnitude 4.5 up until November 4, 2025. There is a notable change in b-value between foreshocks of the Mw 7.4 event and the subsequent aftershock sequence (Figure 8).

In addition, we also model the rate of the occurrence of events during the evolution of the sequence. We fit the Epidemic Type Aftershock Sequence (ETAS) model to the sequence, including both foreshocks and aftershocks of the mainshock. The conditional intensity function  $I(t,H_t)$  of the ETAS model is defined as follows (Ogata, 1988; Harte, 2010):

$$\lambda(t \mid H_t) = \mu + K \sum_{i:t_i < t}^{n(t)} \frac{e^{\alpha (m_i - m_0)}}{\left(\frac{t - t_i}{c} + 1\right)^p},$$
(1),

where m, K, c, p, a are model parameters and  $\mu$  specifies the average background rate of seismicity. The summation term represents the contribution to the total seismicity rate by n(t) preceding events, which is performed over the occurrence of all past events above magnitude  $m_0$  before time t. The parameters are estimated using the maximum likelihood approach.

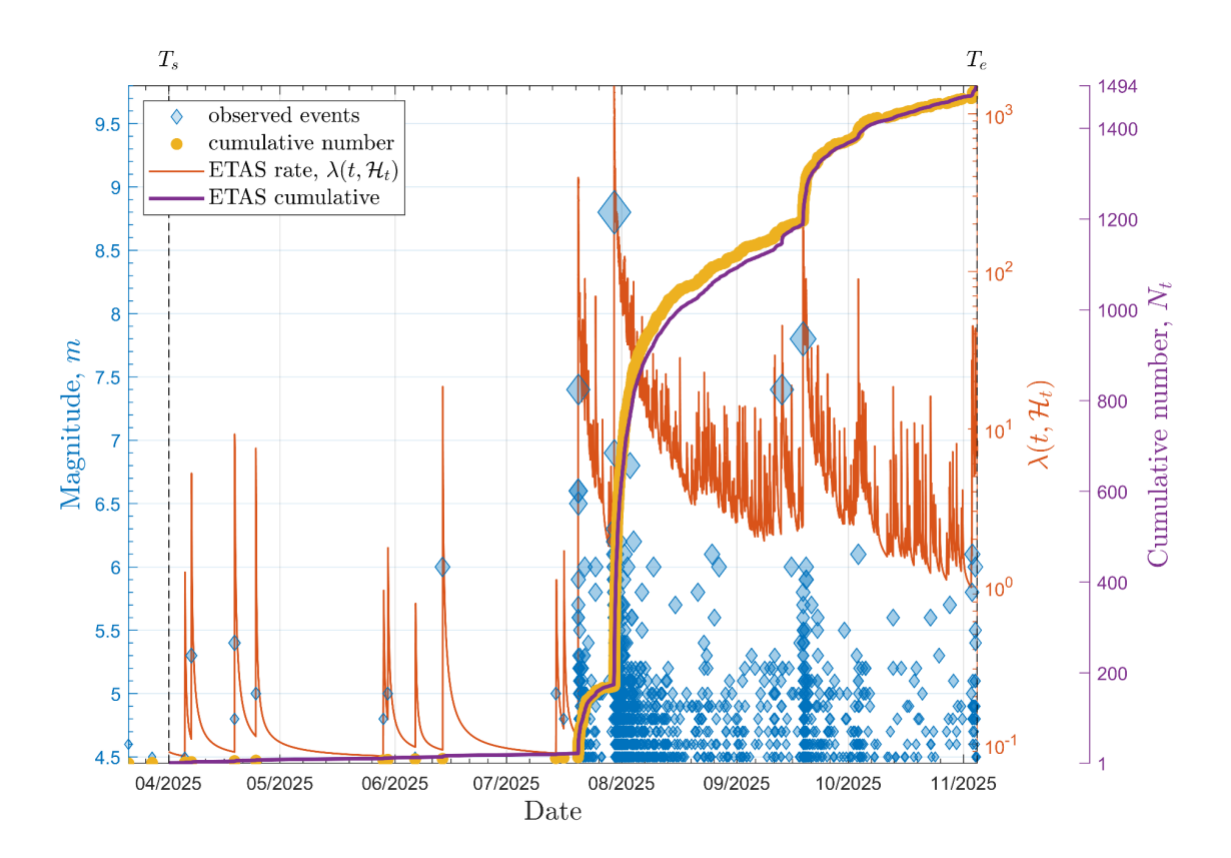


**Figure 9.** The evolution of the 2025 Kamchatka earthquake sequence between April 1 and November 4, 2025. All events above magnitude 4.5 are shown as blue solid rhombus symbols. The fit of the ETAS model is given as a dark orange highly variable curve that gives the estimated conditional seismicity rate,  $I(t, H_t)$ .

The result of the fitting of the ETAS model to the sequence for all events above magnitude 4.5 and during the target time interval  $[T_s, T_e]$  between 1 April 2025 and 4 November 2025, is plotted in Figure 9. We specify a time interval  $[T_0, T_s]$  between 1 March and 1 April 2025, to properly calibrate the rate in the target time interval. The estimated ETAS parameters are [m, K, c, p, a] = [0.08, 6.63, 0.022, 1.29, 1.30]. To illustrate how the ETAS model describes the seismicity rate, we also plot the events and the cumulative numbers in Figure 9. Overall, the model describes the sequence rate reasonably well with a slight underestimation of the rate in the August and September period of the aftershock sequence.

# 7. Waveform Analysis of Event Productivity and Statistical Properties

The above analysis on the foreshock and aftershock behaviors is based on regular or enhanced earthquake catalogs, which are known to be incomplete immediately following the mainshock (Kagan, 2004), even after applying template-matching or machine-learning methods. Recently, several studies directly used amplitude distributions of the high-frequency envelope functions to quantify their statistical behaviors (Sawazaki, 2021; Shearer et al., 2025; Clements et al., 2025), including an attempt to discriminate between potential foreshocks and regular mainshock/aftershock sequences (Lippiello et al., 2025).

Here, we apply two methods to further quantify the statistical properties and event productivity following 5 Mw>7 events (including the Mw 7.4 foreshock and the Mw 8.8 mainshock). In the first method, we use the square sum of the 2-16 Hz band-pass-filtered envelope function to compute the amplitude of completeness  $A_c(t)$  before and after each target event (Clements et al., 2025). We use 5 days of continuous waveforms recorded at station IU.PET for the five events. A 5-day background curve before the 2025 Mw7.4 foreshock was also computed to illustrate the background noise and seismicity variability. Following Clements et al. (2025), we measure  $A_c(t)$  as the 84% percentile of the logarithmic ground motion within a time window T. Here, we use a logarithmic time window length of 0.2, with a logarithmic sliding time window step of 0.01. Figure 10(a) shows that  $A_c(t)$  functions for all 5 target events decay logarithmically with time. However, their productivity levels are different. As expected, the M8.8 curve has the highest productivity. The M7.4 foreshock and the M7.8 aftershock have the second-highest productivity, while the 2024 M7.0 event and the M7.4 aftershocks have the lowest aftershock productivity. Their  $A_c(t)$  curves almost become flat near the end of the analysis time windows.

For comparison, we also compute the seismicity rates following these 5 M7+ events, based on earthquakes listed in the USGS and USGS catalogs. We define the aftershock zones as the 2 times the source radius as determined by the USGS finite-fault solutions for the four M7+

events. For the M8.8 mainshock, we select its aftershock zone as the region immediately surrounding the mainshock rupture from the USGS finite-fault solutions. We also use the sliding data window that begins with 4 aftershocks and ends with 200 aftershocks (Ziv et al., 2003). Figure 10b shows that the aftershocks following the M7.4 foreshock appear to have the highest aftershock productivity within the time scales of hours to days. The aftershock rate of the M8.8 mainshock is in the middle, likely reflecting a significant lack of early aftershocks due to overlapping arrivals (Peng et al., 2007).

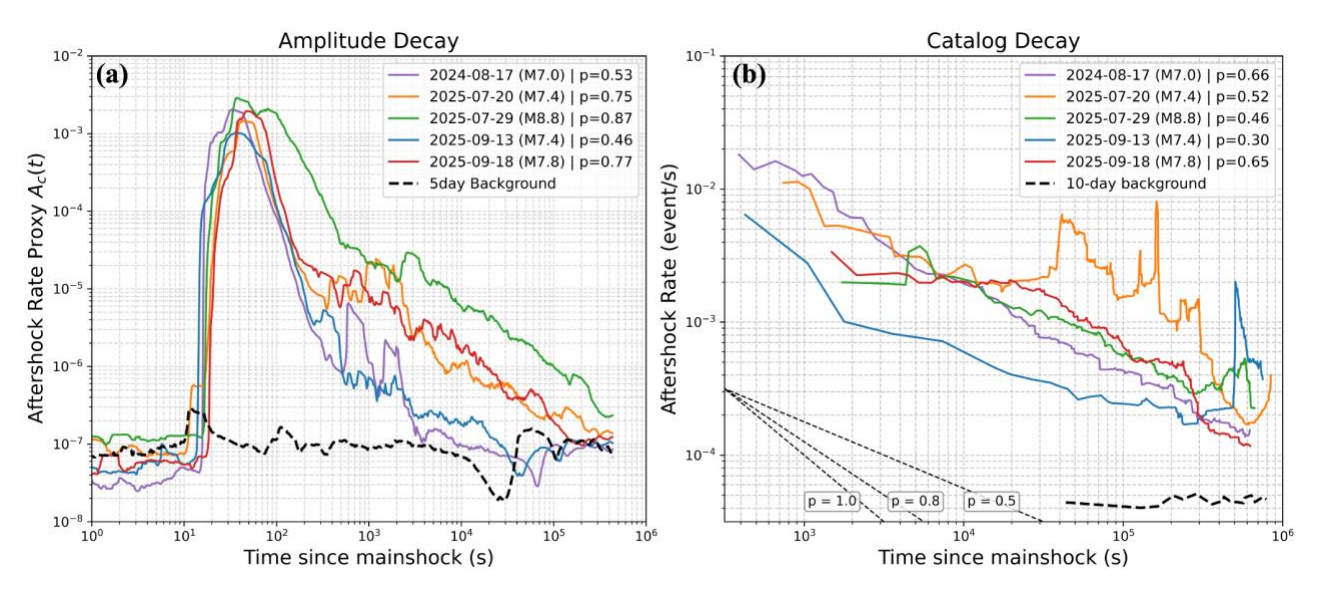


Figure 10. (a) Amplitude of completeness Ac(t) curves for the 5 M7+ sequences. The horizontal dashed lines mark the approximate 5-day background levels before the Mw 7.4 foreshock. (b) Aftershock rate decay for 5 M7+ sequences with M>3 based on GSRAS and USGS catalog. The horizontal dashed lines mark the approximate 10-day background levels before the Mw 7.4 foreshock. The dashed lines mark the Omori-law decay constant p value of 1, 0.8 and 0.5, respectively.

The second method attempts to quantify potential waveform differences and abnormal behaviors between the M7.4 foreshock and the rest 4 M7+ events (Lippiello et al., 2025). We calculate the Q value, which is another measure of the productivity of the sequence (Lippiello et al., 2025), as follows:

 $Q = \frac{n_{obs} K 10^{\delta \mu}}{10^{\beta \mu_M}} \tag{2}$ 

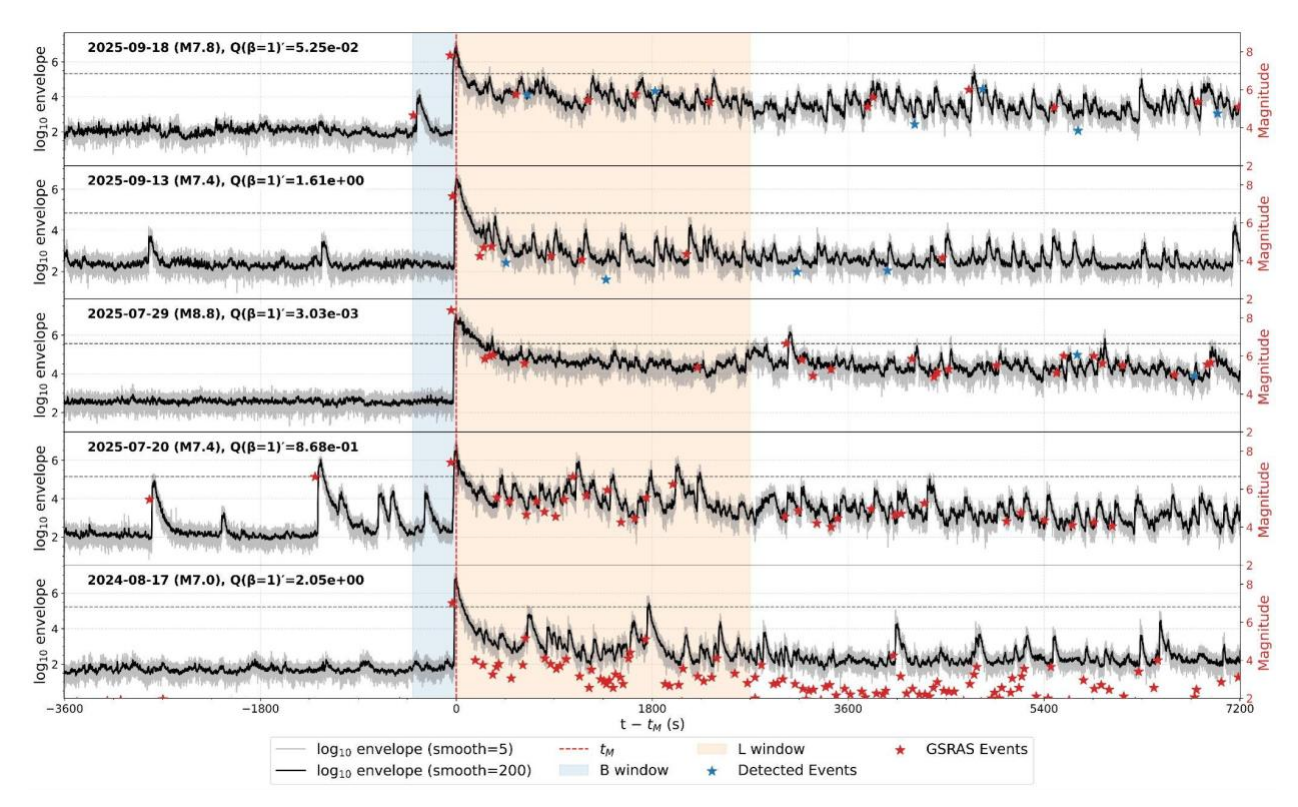
where  $n_{obs}$  is determined following the method of Peng et al. (2007) for  $\mu(t)$  within the first 45 minutes after the mainshock, counted manually. The coefficient K is introduced as described in Lippiello, Petrillo, Godano et al. (2019), and is based on statistical results. Here we use a value of 100. Both  $\delta\mu$  and  $\mu_M$  are obtained from the band-pass-filtered envelopes, using a time window of 400 s before and 45 minutes after the original time, with a smoothing parameter of 5. The parameter  $\beta$  is approximately equal to the b-value of the Gutenberg–Richter law. We consider cases with  $\beta$  = 1.0, 0.8, 0.7, and 0.4. Lippiello et al. (2025) found a possible threshold of Q = 0.18 for selected M>6 events around the world, above which the target event could be considered as a possible foreshock, defined as an earthquake that is followed within 10 days by a larger event within 50 km.

Figure 11 shows the 2-16 Hz band-pass-filtered envelope functions and the corresponding Q values. The case with  $\beta$ =1 corresponds to Q', the Q value without multiplication by  $n_{obs}$  in Equation (2), representing the minimum possible value. Specifically, for the events on 17 August 2024, 20 July 2025, and 13 September 2025, the corresponding Q' values are 2.0, 0.8, and 1.6, respectively. Regardless of the choice of  $n_{obs}$ , these values remain greater than 0.18. For the M7.8 aftershock on 18 September 2025, the number of observed aftershocks ( $n_{obs}$ ) is significantly larger than 8, also leading to Q > 0.18. The only exception is the M8.8 mainshock, whose Q value is relatively small and inconsistent with the observed seismicity. The Q value associated with each  $\beta$  value can be found in Table S1 in the Supplementary.

To further test the general applicability of this method, we extend the calculation to all events with magnitudes larger than 6.0 occurring between 17 August 2024 and 23 September 2025 (Figure 12). In this broader analysis, we set n<sub>obs</sub>=1 and K=1, thereby obtaining the minimum possible Q values. The Q values fluctuate over time and do not show any obvious patterns. For example, the events on 30 August 2024 (M6.1) and 30 September 2024 (M6.2)

were not followed by larger events within 10 days, yet their minimum Q values still exceeded 0.18 (Figure 12).





**Figure 11.** Examples of envelope fitting and Q value calculation for four mainshocks with M > 7. The black curves show the smoothed logarithmic envelopes (smooth sample=5), while the vertical lines indicate the fitting windows for  $\mu_M$ ,  $\mu_B$ , and  $\mu_L$ . The calculated Q values are reported for different β parameters (β = 1.0, 0.8, 0.7, 0.4). These results illustrate that the obtained Q values strongly depend on the assumed β, but even the minimum values (β=1) are significantly larger than the threshold of 0.18 for most events, suggesting that these earthquakes can be considered potential foreshocks.

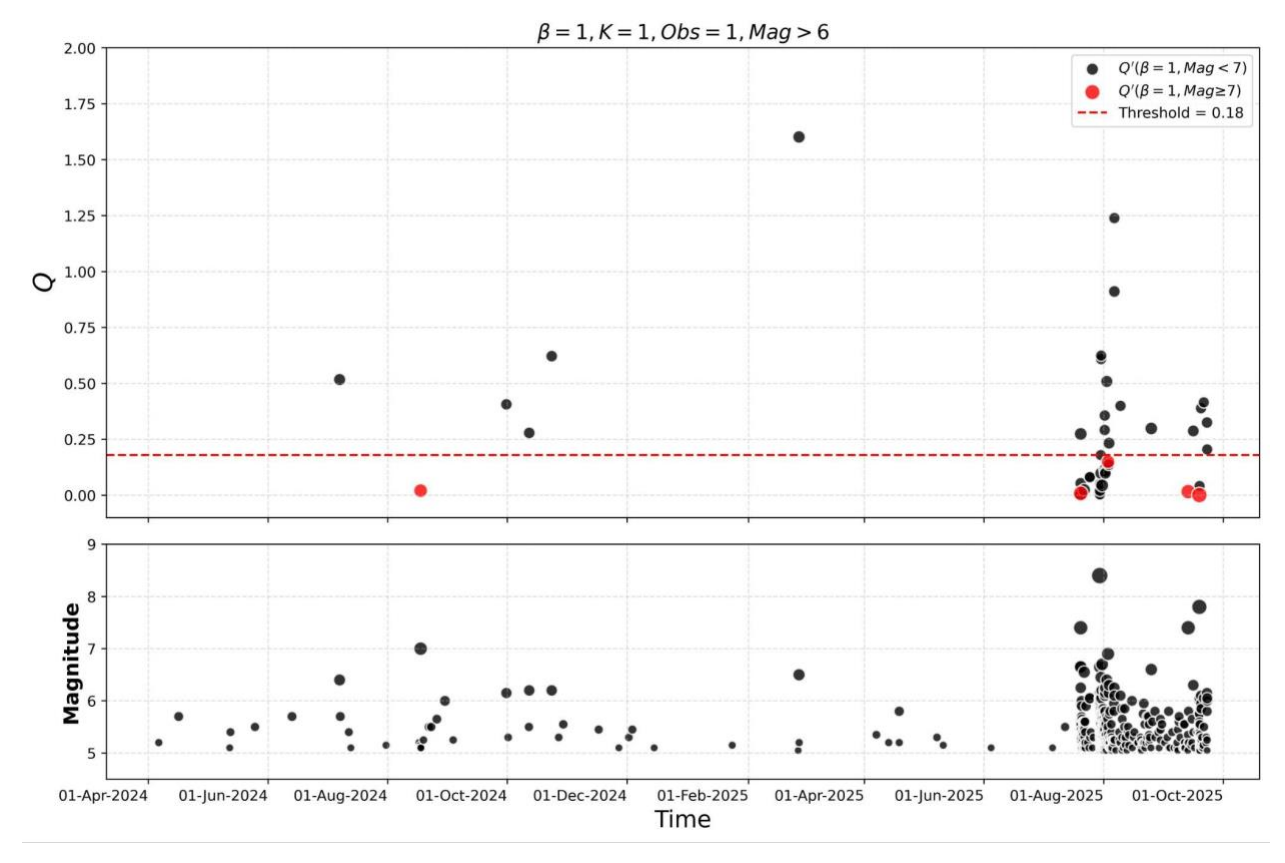


**Figure 12.** Temporal distribution of Q' values for earthquakes with M > 6 between July 2024 and September 2025, calculated with  $\beta$  = 1, K=1, and  $n_{obs}$  =1. Black circles represent events with 6.0 < M < 7.0, and red circles represent events with M > 7.0. The dashed red line marks the threshold of Q = 0.18.

#### 8. Discussion and Conclusions

In this study we present results before, during and after the 29 July 2025 Mw 8.8 Kamchatka earthquake sequence using a combination of multiple approaches and techniques, including one-station template matching with the obtained catalogs, seismicity statistical analysis, teleseismic back-projection, and geodetic constraints. We observe the spatiotemporal evolution from foreshock through early aftershocks of the Mw 8.8 event, with the emphasis on the possibility of afterslip-driven seismicity expansion between the largest foreshock event and the mainshock. We also find a relatively high aftershock productivity of the M7.4 foreshock when compared with other M7+ events in this region.

Here we compare our results of the mainshock rupture properties with other recent studies in this region. Our back-projection of teleseismic P waves from three continental arrays all show a predominant southwest rupture for 500 km over about 220 s, with an average rupture speed near 2.3 km/s. This is largely consistent with other back-projection results (e.g., Xu et al., 2025). Multiple bursts of high-frequency energy are seen with short pauses, consistent with failure of multiple patches on the plate interface obtained from finite-fault modeling (Yagi et al., 2025; Xu et al., 2025). Another robust feature from our and other studies is that the mainshock slip appears to stop near Cape Shipunskiy. The 1952 Mw8.8-9.0 Kamchatka earthquake ruptures shared some similarity to the 2025 event, although the 1952 mainshock slip appears to complement with the 2025 rupture (Mikhailov et al., 2025; Yagi et al., 2025), and its aftershocks showed possible slip northeast of Cape Shipunskiy (MacInnes et al., 2010; Yagi et al., 2025).

Figure 12a shows that, in addition to the 1952 and 2025 mainshocks, other events, such as the 1923 M8.4, 1959 M8.3, and 1971 M7.6 events (Chebrov, 2025), as well as the 2024 M7.0 (Chebrov et al., 2025) and 09/13/2025 M7.4 and 09/19/2025 M7.8 earthquakes, all occurred on either side of Cape Shipunskiy. We argue that the segment near Cape Shipunskiy acts as a "soft barrier" (Wang et al., 2025), where the segment may occasionally stop earthquake rupture from propagating through, but in other cases, it may participate in the rupture or initiate ruptures. Such a soft barrier can exist in the down-dip directions, such as the serpentinized mantle wedge in the Chile subduction zone (Wang et al., 2020, 2025), or in the along-strike directions, such as the possible "soft barrier" is the tip of the Kii Peninsula in the Southwest Japan subduction zone, which separated the 1944 Tonankai Mw 8.1 and the 1946 Nankai Mw 8.4 earthquakes into distinct rupture zones (Ando, 1975; Kodaira et al., 2006). However, in previous earthquake cycles, these adjacent rupture zones either ruptured in one single event (e.g., the 1707 Mw8.7 Hoei earthquake), or two events in the 1854 Ansei great earthquake sequences that were only 31 hrs apart. Bassett and Watts (2015a, 2015b) found negative freeair gravity anomalies in the large earthquake rupture zones surrounding Cape Shipunskiy where an extended continental shelf can be seen from the sea floor bathymetry (Figure 13a). In continental thrust faults, recent studies also revealed potential contributions of the hanging

wall topography and excess weight in controlling the segmentation of large thrust earthquakes such as the 2008 Mw7.9 Wenchuan earthquake (Styron and Hetland, 2015; Tan et al., 2018). These studies highlight the need to better understand the interplay among the geometry and material properties of overriding (and incoming) plates, the frictional properties, and diverse fault-slip behaviors along the plate interface.

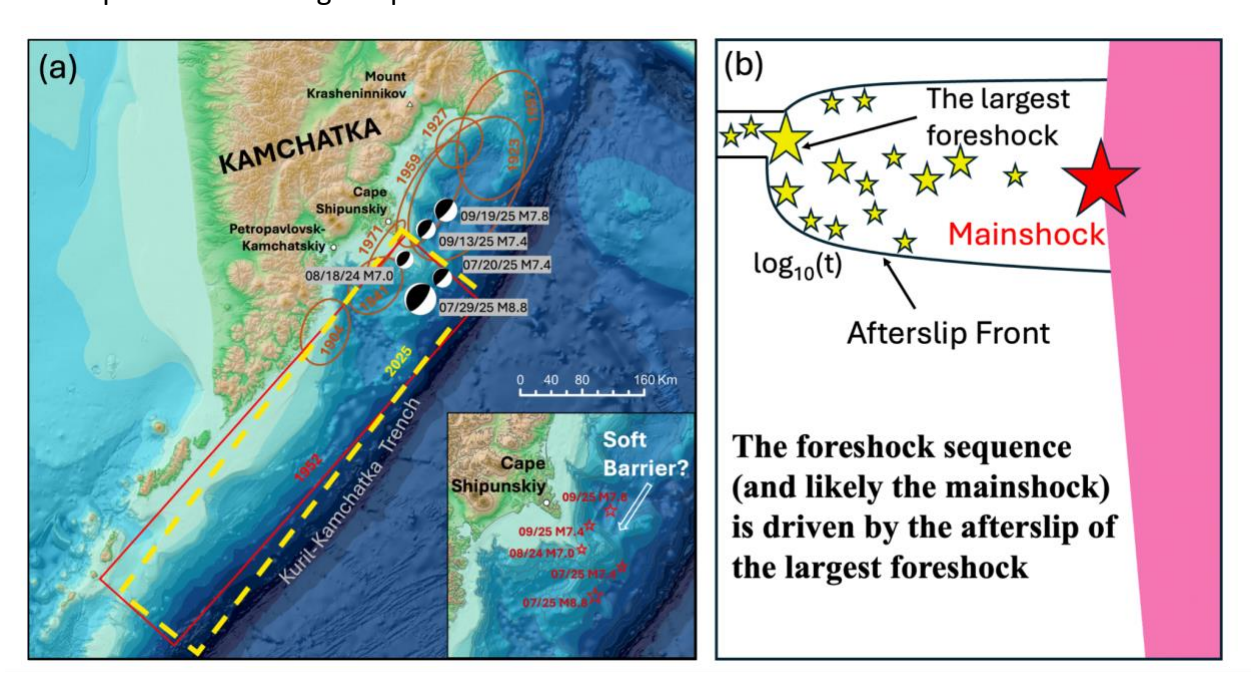


Figure 13. (a) Kamchatka Peninsula map with rupture zones of significant historical earthquakes (orange) with the focus estimated rupture zones of the 1952 event (red) and the 2025 event (dashed yellow). The inset shows zoomed in of Cape Shipuskiy region with 5 mentioned focusing events. (b) The schematic diagram of the proposed foreshock model for the sequence

of the Mw 7.4 foreshock and the Mw 8.8 mainshock.

In this study, we find a clear along-strike expansion of seismicity following the largest foreshock of M7.4 that occurred 10 days before the M8.8 mainshock. The expansion fits the log10(t) function slightly better than the Vt function, which would argue for an afterslip-driven mechanism. At the same time, we also find a similar log10(t) decay in the trench normal displacement following the M7.4 foreshock, consistent with the log10(t)-type aftershock expansion. Hence, we propose yet another foreshock model (Figure 13b) where the largest foreshock and its subsequent afterslip trigger the mainshock nucleation. Note that this model is not new, because similar models, such as the rate-dependent cascade-up model (McLaskey,

2019), have been proposed before. In addition, Noda et al. (2013) have shown that precursory earthquakes (i.e., foreshocks) can be followed by larger afterslip than non-precursory ones. In the migratory slow-slip model (Wang et al., 2024), a migrating slow slip occurs before the largest foreshock. Here, the largest foreshock occurs first, triggers afterslip (likely larger than expected), and then the mainshock. It is possible that slow slip occurred before the M7.4 foreshock, but besides several moderate-size events (M5-6) occurring before, we do not have any additional evidence to argue for the existence of precursory slow slip before the M7.4 foreshock and the M8.8 mainshock. In addition, we find that the M7.4 foreshock was indeed followed by an energetic aftershock sequence with more expansion and higher productivity than the other three M7+ events in the same region. However, the 2024 M7.0 event was smaller and deeper, and the other two events (M7.4 and M7.8) were aftershocks of the M8.8 mainshock, and their properties might also be different. A systematic comparison of similar-sized events in other regions is needed to better establish the uniqueness of this foreshock sequence.

Migrating foreshocks preceding great subduction earthquakes have been documented before the 2011 M9.1 Tohoku-Oki and 2014 M8.1 Iquique earthquakes (Kato et al., 2012, 2014; Ruiz et al., 2014). In both cases, slow slip was invoked as the driving mechanism for the foreshock migration and mainshock nucleation, and geodetic instruments also recorded both long and short-term slow slip signals (Ito et al., 2013; Ruiz et al., 2014), although the 2-hourlong precursory slip before the 2011 Tohoku-Oki and other large earthquakes is still in debate (Bletery and Nocquet, 2023, 2025; Hirose et al., 2024). However, we expect that moderate to large foreshocks are followed by its own aftershocks that expand with time, which are likely triggered by afterslip that propagates outwards following the log10(t) expansion (Kato, 2007; Peng and Zhao, 2009), as well as decaying with time similar to the Omori's law aftershock decay (Perfettini and Avouac, 2004, 2007; Hsu et al., 2006; Utsu et al., 1995). Other stress-triggering mechanisms can also trigger aftershocks (Freed, 2005). Hence, the presence of the expanding aftershocks and afterslip following a moderate-to-large earthquake is not enough to guarantee that it will be followed by a larger event. However, one can potentially examine whether the

expanding speed and region of aftershocks following the M7.4 foreshock (and other foreshocks such as the 2011 M7.3 foreshock before the M9.1 Tohoku-Oki earthquake) is abnormal or not.

In recent years, multiple methods have been used to study whether a large event is a mainshock itself or a foreshock to a larger event by investigating the sequence statistical behavior, which includes tracking the changes in b-value, amplitude of completeness, and calculating the immediate envelope-based productivity Q (Schorlemmer et al., 2005; Nanjo et al., 2012; Gulia and Wiemer, 2019; Lippiello et al., 2019; Lippiello et al., 2025). In this Kamchatka sequence, an increase in b-value is observed from the background before the Mw 7.4 foreshock window to the aftershocks of the Mw 8.8 mainshock (Figure 8). This is different with the interpretation of a drop in b-value drop during a potential foreshock sequence (Gulia and Wiemer, 2019). The largest change in the b value occurred before and after the mainshock (Figure 8). However, a change in b value around the mainshock is somewhat expected, which can be caused by a combination of factors such as changes in the magnitude of completeness (Mc) or changes in the differential stress levels following the mainshock (Tormann et al., 2015; Gulia and Wiemer, 2019; van der Elst, 2021; Ito and Kaneko, 2023). We do not attempt to compute a more fine-scale changes in b-value in this study, mainly because the catalog we have obtained (a combined local GSRAS catalog and a single-station template-matching catalog) still misses many aftershocks, especially immediately following the M7.4 foreshock and the M8.8 mainshock (Figure 5).

Our amplitude-decay analysis result shows consistent Omori's law-type decay pattern but highlights different productivity rankings with the M8.8 sequence dominating in the amplitude proxy because many early aftershocks overlap and elevate the envelope level (Figure 10). The M7.4 foreshock appears to be the second most productive, with its aftershock levels matching that from the M7.8 aftershock. High foreshock productivity is often followed by enhanced short-term aftershock productivity, consistent with a cascade-type response of the system (Marsan et al., 2014). A transient aseismic slip can further amplify this pattern, as documented for the 2017 Valparaiso sequence (Moutote et al., 2023). This observation is consistent with the finding by Stein et al. (2025), indicating that more productive moderate-size earthquake sequences may have higher potential to become a foreshock sequence (Wetzler et

al., 2023). In the Q calculation, our results show a consistency with a strong early productivity sequence, where events exceed the Q > 0.18 threshold with reasonable choices of  $\beta$  and window (Peng et al., 2007; Lippiello et al., 2019; Lippiello et al., 2025). However, this method shows several false positives when extending the same calculation to many M6 to M7 events in this sequence (Figure 12). We argue that the Q analysis (Lippiello et al., 2025) is sensitive to  $\beta$ , the early time count, and completeness in the first few hours, which cannot be easily applied in a real-time setting to discriminate between real foreshocks from normal earthquake sequences.

581

582

583

584

585

586

587

588

589

590

591

592

593

594

595

596

597

598

599

600

601

602

603

604

605

606

607

Our preliminary results are affected by the limitation of the data availability and station coverage. Continuous waveforms were available from one nearby broadband station only (IU.PET), and only one GNSS station (PETT) had accessible 5-min displacement recording. The matched-filter detections are limited by the template event from the obtained catalog, in which the absolute locations of detected events remain uncertain due to the assignment of template locations. In addition, the number of new detected events is not significant compared to those with more station coverage (Peng and Zhao, 2009; Neves et al., 2024), as it is a challenge to achieve all the hidden events from one station's waveforms. Although the GNSS record has a high sampling rate (5-minute per sample), it is still a limitation to observe any immediate change in displacement within short time window right before the Mw 8.8 mainshock, which is essential to observe any precursory signals large earthquake (Bletery and Nocquet, 2023). To further improve this study, a more complete continuous seismic and geodetic data coverage is required to build a high-resolution catalog. Combining with multi-station geodetic recordings and other geophysical observations (Shelly, 2024), the physical mechanisms of the foreshock generation and mainshock nucleation can be better refined (Peng and Lei, 2025). Accurately identifying those sequences with abnormal behaviors can help to improve our ability to forecast short-term low-probability events (Hardebeck et al., 2024), which is essential for operational earthquake forecasting (Jordan et al., 2011; Goltz, 2025).

Taken together, the observations support a segmented rupture on the Kuril-Kamchatka interface and a plausible afterslip between the Mw 7.4 foreshock and the Mw 8.8 mainshock

within the limits of the available data. Back projection, the enhanced catalog, and the geodetic record give a consistent picture of southwest directivity, with several sub-events rupturing during the mainshock, and a deficit of seismic activity to the northeast of the mainshock hypocenter. The Q values and the change in b value summarize the strong immediate productivity of the largest events and are used here as descriptive indicators rather than predictors. This combined approach sets a clear starting point for further analysis such as high-resolution seismicity and subduction-zone imaging, updated finite fault models for this unique earthquake sequence, afterslip and other postseismic deformation and potential pre-seismic slip, and forecasting of future large earthquakes in this and other subduction zones.

### Acknowledgements

We acknowledge Prof. Aleksey A. Emanov's enthusiastic approach to accessing the current seismicity catalogs of the Kamchatka Branch of Geophysical Survey, RAS, Petropavlovsk-Kamchatsky, Russia, for providing permission to the local earthquake catalog. The manuscript benefits from comments by Professors Jing Wu and Yangfan Deng. P.M., X.S., C.D. and Z.P. are partially supported by U.S. National Science Foundation grant RISE-2425889. Tuncay Taymaz thanks Istanbul Technical University (ITU-BAP) and Disaster Management Institute (ITU-AYE) for allocating research funds and environment during the recent hectic and chaotic years.

#### References

- Ammon, C., H. Kanamori, and T. Lay, 2008. A great earthquake doublet and seismic stress transfer cycle in the central Kuril Islands. Nature, 451, 561–565.
- 630 https://doi.org/10.1038/nature06521

Ando, M., 1975. Source mechanisms and tectonic significance of historical earthquakes along the Nankai Trough, Japan. Tectonophysics, 27(2), 119-140. https://doi.org/10.1016/0040-1951(75)90102-X

636 Bassett, D., and A. B. Watts, 2015a. Gravity anomalies, crustal structure, and seismicity at 637 subduction zones: 1. Seafloor roughness and subducting relief, Geochem. Geophys. Geosyst., 638 16, 1508-1540, doi:10.1002/2014GC005684. 639 640 Bassett, D., and A. B. Watts, 2015b. Gravity anomalies, crustal structure, and seismicity at 641 subduction zones: 2. Interrelationships between fore-arc structure and seismogenic behavior, 642 Geochem. Geophys. Geosyst., 16, 1541–1576, doi:10.1002/2014GC005685. 643 644 Beroza, G. C., M. Segou, and W. L. Ellsworth, 2021. Machine learning and earthquake 645 forecasting—next steps. Nature Communications, 12, 4761. https://doi.org/10.1038/s41467-021-24952-6 646 647 648 Bilek, S. L., and T. Lay, 2018. Subduction zone megathrust earthquakes. Geosphere, 14(4), 649 1468-1500. https://doi.org/10.1130/GES01608.1 650 651 Bletery, Q. and Nocquet, J.M., 2023. The precursory phase of large earthquakes. Science, 652 381(6655), pp.297-301. https://doi.org/10.1126/science.adg2565 653 654 Bletery, Q., & Nocquet, J.-M., 2025. Do large earthquakes start with a precursory phase of slow 655 slip?. Seismica, 3(2). https://doi.org/10.26443/seismica.v3i2.1383 656 657 Bouchon, M., V. Durand, D. Marsan, H. Karabulut, and J. Schmittbuhl, 2013. The long precursory 658 phase of most large interplate earthquakes. Nature Geoscience, 6, 299–302. 659 https://doi.org/10.1038/ngeo1770. 660 661 Bradley, K., and J. Hubbard, 2024. M7.1 strikes offshore Kamchatka – in an area that nucleated a M9 in 1952. Earthquake Insights. https://doi.org/10.62481/33403660 662

664 Bradley, K., Hubbard, J., 2025a. A first look at the Mw8.8 Kamchatka earthquake. Earthquake 665 Insights, https://doi.org/10.62481/f8aeb017 666 667 Bradley, K., Hubbard, J., 2025b. M 7.8 strikes offshore Kamchatka. Earthquake Insights, 668 https://doi.org/10.62481/98dfff39 669 670 Chebrov, D., 2025. The Kamchatka Earthquake of 2025, M8.8: Results from Regional Data 671 Processing. A presentation at the SnT2025 CTBT: Science and Technology Conference 2025, 672 Vienna. 673 674 Chebrov, D.V., Matveenko, E.A., Abubakirov, I.R., Droznina, S.Y., Lander, A.V., Mityushkina, S.V., 675 Pavlov, V.M., Raevskaya, A.A., Saltykov, V.A., Senyukov, S.L. and Titkov, N.N., 2025. The MW 7.0 676 Shipunsky Earthquake of August 17, 2024 off the East Coast of Kamchatka. Journal of 677 Volcanology and Seismology, 19(3), 271-280. https://doi.org/10.1134/S0742046325700101 678 679 Clements, T., E. S. Cochran, S. E. Minson, N. J. van der Elst, C. E. Yoon, A. Baltay, and M. T. Page, 680 2025. Mechanics and statistics of postseismic shaking. Geophysical Research Letters, 52, 681 e2025GL116673. https://doi.org/10.1029/2025GL116673 682 683 DeMets, C., R. G. Gordon, and D. F. Argus, 2010. Geologically current plate motions. 684 Geophysical Journal International, 181(1), 1–80. https://doi.org/10.1111/j.1365-685 246X.2009.04491.x 686 687 Eggert, S., and T. R. Walter, 2009. Volcanic activity before and after large tectonic earthquakes: 688 observations and statistical significance. Tectonophysics, 471(1–2), 14–26. 689 https://doi.org/10.1016/j.tecto.2008.10.003

691 Freed, A.M., 2005. Earthquake triggering by static, dynamic, and postseismic stress transfer. 692 Annu. Rev. Earth Planet. Sci., 33(1), 335-367. 693 https://doi.org/10.1146/annurev.earth.33.092203.122505 694 695 Fan, W., and P. M. Shearer, 2017. Investigation of backprojection uncertainties with M6 696 earthquakes. Journal of Geophysical Research: Solid Earth, 122, 7966–7986. 697 https://doi.org/10.1002/2017JB014495 698 699 Gibbons, S. J., and F. Ringdal, 2006. The detection of low-magnitude seismic events using array-700 based waveform correlation. Geophysical Journal International, 165(1), 149–166. 701 https://doi.org/10.1111/j.1365-246X.2006.02865.x 702 703 Global Volcanism Program (GVP), 2025. Kamchatka Volcano Activity Reports. Smithsonian 704 Institution. https://volcano.si.edu/ (accessed 2 October 2025) 705 706 Goltz, J.D., 2025. Are Short-Term Low-Probability Earthquake Forecasts Useful? An Emergency 707 Management Perspective. Seismological Research Letters. 708 https://doi.org/10.1785/0220250273 709 710 Gulia, L., & Wiemer, S., 2019. Real-time discrimination of earthquake foreshocks and 711 aftershocks. Nature, 574, 193-199. https://doi.org/10.1038/s41586-019-1606-4 712 713 Gutenberg, B., and Richter, C. F., 1944. Frequency of earthquakes in California. Bulletin of the 714 Seismological Society of America. https://doi.org/10.1785/BSSA0340040185 715 716 Hainzl, S., 2004. Seismicity patterns of earthquake swarms due to fluid intrusion and stress 717 triggering. Geophysical Journal International, 159(3), 1090–1096. 718 https://doi.org/10.1111/j.1365-246X.2004.02463.x

- Hardebeck, J.L., Llenos, A.L., Michael, A.J., Page, M.T., Schneider, M. and van der Elst, N.J., 2024.
- 721 Aftershock forecasting. Annual Review of Earth and Planetary Sciences, 52, 61-84.
- 722 https://doi.org/10.1146/annurev-earth-040522-102129

723

- Harte, D., 2010. PtProcess: An R package for modelling marked point processes indexed by
- 725 time. Journal of Statistical Software, 35(8), 1–32. https://doi.org/10.18637/jss.v035.i08

726

- Hayes, G. P., G. L. Moore, D. E. Portner, M. Hearne, H. Flamme, M. Furtney, and G. M. Smoczyk,
- 728 2018. Slab2, a comprehensive subduction zone geometry model. Science, 362(6410), 58–61.
- 729 https://doi.org/10.1126/science.aat4723

730

- Hirose, H., Kato, A., & Kimura, T. (2024). Did short-term preseismic crustal deformation precede
- 732 the 2011 great Tohoku-oki earthquake? An examination of stacked tilt records. Geophysical
- 733 Research Letters, 51, e2024GL109384. https://doi.org/10.1029/2024GL109384

734

- Hsu, Y.-J., M. Simons, J.-P. Avouac, J. Galetzka, K. Sieh, M. Chlieh, D. Natawidjaja, L.
- 736 Prawirodirdjo, and Y. Bock, 2006. Frictional afterslip following the 2005 Nias–Simeulue
- 737 earthquake, Sumatra. Science, 312(5782), 1921–1926.
- 738 https://doi.org/10.1126/science.1126960

739

- Hubbard, J. and Bradley, K., 2025a. M7.4 earthquake strikes the Kamchatka Peninsula.
- 741 Earthquake Insights, https://doi.org/10.62481/a8be96de

742

- Hubbard, J. and Bradley, K., 2025b. Updates on the Kamchatka earthquake. Earthquake
- 744 Insights, https://doi.org/10.62481/69d32d61

745

- Hubbard, J. and Bradley, K., 2025c. M7.4 earthquake shakes Kamchatka: largest aftershock of
- 747 the M8.8 earthquake. Earthquake Insights, https://doi.org/10.62481/b32675e0

- 749 Ito, Y., Hino, R., Kido, M., Fujimoto, H., Osada, Y., Inazu, D., Ohta, Y., Iinuma, T., Ohzono, M.,
- 750 Miura, S. and Mishina, M., 2013. Episodic slow slip events in the Japan subduction zone before
- 751 the 2011 Tohoku-Oki earthquake. Tectonophysics, 600, 14-26.
- 752 https://doi.org/10.1016/j.tecto.2012.08.022

753

- 754 Ito, R., Y. Kaneko, 2023. Physical mechanism for a temporal decrease of the Gutenberg–Richter
- 755 b-value prior to a large earthquake. Journal of Geophysical Research: Solid Earth, 128,
- 756 e2023JB027413. https://doi.org/10.1029/2023JB027413

757

- Jordan, T.H., Chen, Y.T., Gasparini, P., Madariaga, R., Main, I., Marzocchi, W., Papadopoulos, G.,
- 759 Sobolev, G., Yamaoka, K. and Zschau, J., 2011. Operational earthquake forecasting: State of
- 760 knowledge and guidelines for utilization. Annals of Geophysics, 54(4), 315-391.
- 761 https://doi.org/10.4401/ag-5350

762

- 763 Kagan, Y. Y., 2004. Short-term properties of earthquake catalogs and models of earthquake
- 764 source. Bulletin of the Seismological Society of America, 94(4), 1207–1228.
- 765 https://doi.org/10.1785/012003098

766

- Johnson, J., and K. Satake, 1999. Asperity distribution of the 1952 great Kamchatka earthquake
- and its relation to future earthquake potential in Kamchatka. Pure and Applied Geophysics, 154,
- 769 541–553. https://doi.org/10.1007/s000240050243

770

- 771 Kato, A., K. Obara, T. Igarashi, H. Tsuruoka, S. Nakagawa, and N. Hirata, 2012. Propagation of
- 35 slow slip leading up to the 2011 Mw 9.0 Tohoku-Oki earthquake. Science, 335(6069), 705–708.
- 773 https://doi.org/10.1126/science.1215141

- 775 Kato, A., and S. Nakagawa, 2014. Multiple slow-slip events during a foreshock sequence of the
- 776 2014 Iquique, Chile Mw 8.1 earthquake. Geophysical Research Letters, 41, 5420–5427.
- 777 https://doi.org/10.1002/2014GL061138

778 779 Kato, N., 2007. Expansion of aftershock areas caused by propagating post-seismic sliding. 780 Geophysical Journal International, 168(2), 797–808. https://doi.org/10.1111/j.1365-781 246X.2006.03255.x 782 783 King, G. C. P., R. S. Stein, and J. Lin, 1994. Static stress changes and the triggering of 784 earthquakes. Bulletin of the Seismological Society of America, 84(3), 935–953. 785 https://doi.org/10.1785/BSSA0840030935 786 787 Kiser, E., and M. Ishii, 2017. Back-projection imaging of earthquakes. Annual Review of Earth 788 and Planetary Sciences, 45, 271–299. https://doi.org/10.1146/annurev-earth-063016-015801 789 790 Kodaira, S., T. Hori, A. Ito, S. Miura, G. Fujie, J.-O. Park, T. Baba, H. Sakaguchi, and Y. Kaneda 791 (2006), A cause of rupture segmentation and synchronization in the Nankai trough revealed by 792 seismic imaging and numerical simulation, J. Geophys. Res., 111, B09301, 793 doi:10.1029/2005JB004030. 794 795 Lippiello, E., G. Petrillo, C. Godano, A. Tramelli, E. Papadimitriou, and V. Karakostas, 2019. 796 Forecasting of the first-hour aftershocks by means of the perceived magnitude. Nature 797 Communications, 10, 2953. https://doi.org/10.1038/s41467-019-10763-3 798 799 Lippiello, E., G. Petrillo, C. Godano, and L. Dal Zilio, 2025. Toward recognizing the waveform of 800 foreshocks. Geophysical Research Letters, 52, e2025GL115466. 801 https://doi.org/10.1029/2025GL115466 802 803 MacInnes, B. T., R. Weiss, J. Bourgeois, and T. K. Pinegina, 2010. Slip distribution of the 1952 804 Kamchatka great earthquake based on near-field tsunami deposits and historical records. 805 Bulletin of the Seismological Society of America, 100(4), 1695–1709. 806 https://doi.org/10.1785/0120090376

807	
808	Manga, M., and Brodsky, E. E., 2006. Seismic triggering of eruptions in the far field: Volcanoes
809	and geysers. Annual Review of Earth and Planetary Sciences, 34, 263–291.
810	https://doi.org/10.1146/annurev.earth.34.031405.125125
811	
812	Marsan, D., A. Helmstetter, M. Bouchon, and P. Dublanchet, 2014. Foreshock activity related to
813	enhanced aftershock production: Foreshock and aftershock activities. Geophysical Research
814	Letters, 41(19), 6652-6658. https://doi.org/10.1002/2014GL061219
815	
816	Martínez-Garzón, P., and P. Poli, 2024. Cascade and pre-slip models oversimplify the complexity
817	of earthquake preparation in nature. Communications Earth & Environment, 5, 120.
818	https://doi.org/10.1038/s43247-024-01285-y
819	
820	McLaskey, G.C., 2019. Earthquake initiation from laboratory observations and implications for
821	foreshocks. J. Geophys. Res., 124(12), 12882-12904. https://doi.org/10.1029/2019JB018363
822	
823	Mikhailov, V.O., Konvisar, A.M., Smirnov, V.B., Timoshkina, E.P., Titkov, N.N., Khairetdinov, S.A.
824	and Chebrov, D.V., 2025, December. The Rupture Surface Model of the July 29, 2025 M w 8.8
825	Kamchatka Earthquake Based on Satellite Geodesy and Interferometry Data. IDokl. Earth Sc.
826	525, 35. https://doi.org/10.1134/S1028334X25608752
827	
828	Moutote, L., Y. Itoh, O. Lengliné, Z. Duputel, and A. Socquet, 2023. Evidence of a transient
829	aseismic slip driving the 2017 Valparaiso earthquake sequence, from foreshocks to aftershocks.
830	Journal of Geophysical Research: Solid Earth, 128, e2023JB026603.
831	https://doi.org/10.1029/2023JB026603
832	
833	Nanjo, K. Z., N. Hirata, K. Obara, and K. Kasahara, 2012. Decade-scale decrease in b value prior
834	to the M9-class 2011 Tohoku and 2004 Sumatra quakes. Geophysical Research Letters, 39,
835	120304 https://doi.org/10.1029/2012GL052997

836	
837	Neves, M., L. Y. Chuang, W. Li, et al., 2024. Complex rupture dynamics of the extremely shallow
838	August 2020 M5.1 Sparta, North Carolina earthquake. Communications Earth & Environment, 5,
839	163. https://doi.org/10.1038/s43247-024-01316-8
840	
841	Noda, H., M. Nakatani, and T. Hori (2013), Large nucleation before large earthquakes is
842	sometimes skipped due to cascade-up—Implications from a rate and state simulation of faults
843	with hierarchical asperities, J. Geophys. Res., 118, 2924–2952,
844	https://doi.org/10.1002/jgrb.50211.
845	
846	Ogata, Y., 1988. Statistical models for earthquake occurrences and residual analysis for point
847	processes. Journal of the American Statistical Association, 83(401), 9–27.
848	https://doi.org/10.1080/01621459.1988.10478560
849	
850	Peng, Z., and P. Zhao, 2009. Migration of early aftershocks following the 2004 Parkfield
851	earthquake. Nature Geoscience, 2(12), 877–881. https://doi.org/10.1038/ngeo697
852	
853	Peng, Z., J. E. Vidale, M. Ishii, and A. Helmstetter, 2007. Seismicity rate immediately before and
854	after main shock rupture from high-frequency waveforms in Japan. Journal of Geophysical
855	Research: Solid Earth, 112, B03306. https://doi.org/10.1029/2006JB004386
856	
857	Peng, Z., and X. Lei, 2025. Physical mechanisms of earthquake nucleation and foreshock:
858	Cascade triggering, aseismic slip, or fluid flows? Earthquake Research Advances, 5(2), 100349.
859	https://doi.org/10.1016/j.eqrea.2024.100349
860	
861	Peng, Z., X. Lei, D. Wang, X. Si, P. Mach, Q. Zhong, C. Ding, Y. Deng, M. Qin, and S. Miao, 2025.
862	Mainshock rupture properties, aftershock activities and remotely triggered seismicity
863	associated with the 2025 Mw 7.7 Sagaing fault earthquake in Myanmar. Earthquake Research
864	Advances, 5(4), 100413. https://doi.org/10.1016/j.eqrea.2025.100413

865 866 Peng, Z., X. Lei, Q.-Y. Wang, D. Wang, P. Mach, D. Yao, A. Kato, K. Obara, and M. Campillo, 2025. 867 The evolution process between the earthquake swarm beneath the Noto Peninsula, central 868 Japan and the 2024 M 7.6 Noto Hanto earthquake sequence. Earthquake Research Advances, 869 5(1), 100332. https://doi.org/10.1016/j.eqrea.2024.100332 870 Perfettini, H., and J.-P. Avouac, 2004. Postseismic relaxation driven by brittle creep: A possible 871 872 mechanism to reconcile geodetic measurements and the decay rate of aftershocks, application 873 to the Chi-Chi earthquake, Taiwan. Journal of Geophysical Research: Solid Earth, 109, B02304. https://doi.org/10.1029/2003JB002488 874 875 876 Perfettini, H., and J.-P. Avouac, 2007. Modeling afterslip and aftershocks following the 1992 877 Landers earthquake. Journal of Geophysical Research: Solid Earth, 112, B07409. 878 https://doi.org/10.1029/2006JB004399 879 880 Rodkin, MV., T.S Irmak, T. Taymaz, E.V Liperovskaya, 2025. Typical Precursor Anomalies of the 881 February 6, 2023, Mw 7.8 and Mw 7.6 Kahramanmaraş Earthquake Doublet, Turkey, and the 882 Mw 9.0+ Andaman-Sumatra and Tohoku, Japan Mega-Earthquakes Izvestiya - Physics of the 883 Solid Earth, 61(4), 575-585. 884 885 Roeloffs, E., 2006. Evidence for aseismic deformation rate changes prior to earthquakes. Annual 886 Review of Earth and Planetary Sciences, 34, 591–627. 887 https://doi.org/10.1146/annurev.earth.34.031405.124947 888 889 Ross, Z. E., C. Rollins, E. S. Cochran, E. Hauksson, J.-P. Avouac, and Y. Ben-Zion, 2017. 890 Aftershocks driven by afterslip and fluid pressure sweeping through a fault-fracture mesh. 891 Geophysical Research Letters, 44, 8260-8267. https://doi.org/10.1002/2017GL074634 892

893 Ross, Z. E., B. Idini, Z. Jia, O. L. Stephenson, M. Zhong, X. Wang, Z. Zhan, M. Simons, E. J. 894 Fielding, S-H Yun, E. Hauksson, A. W. Moore, Z. Liu, and J. Jung, 2019. Hierarchical interlocked 895 orthogonal faulting in the 2019 Ridgecrest earthquake sequence. Science, 366(6463), 346-351. 896 https://doi.org/10.1126/science.aaz0109 897 898 Ruiz, S., M. Métois, A. Fuenzalida, J. Ruiz, F. Leyton, R. Grandin, C. Vigny, R. Madariaga, and J. 899 Campos, 2014. Intense foreshocks and a slow slip event preceded the 2014 Iquique Mw 8.1 900 earthquake. Science, 345(6201), 1165–1169. https://doi.org/10.1126/science.1256074 901 902 Ruppert, N. A., J. M. Lees, and N. P. Kozyreva, 2007. Seismicity, earthquakes and structure along 903 the Alaska-Aleutian and Kamchatka-Kurile subduction zones: A review. In Volcanism and 904 Subduction: The Kamchatka Region (eds. J. Eichelberger, E. Gordeev, P. Izbekov, M. Kasahara, 905 and J. Lees). https://doi.org/10.1029/172GM12 906 907 Sawazaki, K., 2021. Early forecast of maximum amplitude due to aftershocks by applying 908 extreme value statistics to a single continuous seismogram. Bulletin of the Seismological Society 909 of America, 111(5), 2825–2845. https://doi.org/10.1785/0120200365 910 911 Schorlemmer, D., S. Wiemer, and M. Wyss, 2005. Variations in earthquake-size distribution 912 across different stress regimes. Nature, 437, 539-542. https://doi.org/10.1038/nature04094 913 914 Shapiro, S. A., E. Huenges, and G. Borm, 1997. Estimating the crust permeability from fluid-915 injection-induced seismic emission at the KTB site. Geophysical Journal International, 131(2), 916 F15-F18. https://doi.org/10.1111/j.1365-246X.1997.tb01215.x 917 918 Shcherbakov, R., and D.L. Turcotte, 2004. A modified form of Båth's law, Bulletin of the 919 Seismological Society of America 94 (5), 1968-1975. https://doi.org/10.1785/012003162

921 Shearer, P. M., and N. Shakibay Senobari, 2025. Continuous aftershock hum for over ten days 922 following the 2019 Ridgecrest, California, earthquakes observed with borehole seismometers. 923 Seismological Research Letters, 96(5), 2968-2978. https://doi.org/10.1785/0220250017 924 925 Shelly, D. R., 2024. Examining the connections between earthquake swarms, crustal fluids, and 926 large earthquakes in the context of the 2020–2024 Noto Peninsula, Japan, earthquake 927 sequence. Geophysical Research Letters, 51, e2023GL107897. 928 https://doi.org/10.1029/2023GL107897 929 930 Sheng, Y., A. Mordret, K. Sager, F. Brenguier, P. Boué, B. Rousset, et al., 2022. Monitoring 931 seismic velocity changes across the San Jacinto Fault using train-generated seismic tremors. 932 Geophysical Research Letters, 49, e2022GL098509. https://doi.org/10.1029/2022GL098509 933 934 Stein, R. S., Toda, S., Lotto, G., Gonzalez-Huizar, H., and Sevilgen, V., 2025, Huge July 2025 935 Kamchatka earthquake followed unusually productive foreshock sequence, Temblor, 936 http://doi.org/10.32858/temblor.366 937 938 Styron, R.H. and Hetland, E.A., 2015. The weight of the mountains: Constraints on tectonic 939 stress, friction, and fluid pressure in the 2008 Wenchuan earthquake from estimates of 940 topographic loading. Journal of Geophysical Research, 120(4), 2697-2716. 941 https://doi.org/10.1002/2014JB011338 942 943 Tan, X., Yue, H., Liu, Y., Xu, X., Shi, F., Xu, C., Ren, Z., Shyu, J.B.H., Lu, R. and Hao, H., 2018. 944 Topographic loads modified by fluvial incision impact fault activity in the Longmenshan thrust 945 belt, eastern margin of the Tibetan Plateau. Tectonics, 37(9), 3001-3017. 946 https://doi.org/10.1029/2017TC004864 947

948 Tormann, T., B. Enescu, J. Woessner, et al., 2015. Randomness of megathrust earthquakes 949 implied by rapid stress recovery after the Japan earthquake. Nature Geoscience, 8, 152–158. 950 https://doi.org/10.1038/ngeo2343 951 952 Utsu, T., Y. Ogata, and R. S. Matsu'ura, 1995. The centenary of the Omori formula for a decay 953 law of aftershock activity. Journal of Physics of the Earth, 43(1), 1–33. 954 https://doi.org/10.4294/jpe1952.43.1 955 956 van der Elst, N. J., 2021. B-positive: A robust estimator of aftershock magnitude distribution in transiently incomplete catalogs. Journal of Geophysical Research: Solid Earth, 126, 957 958 e2020JB021027. https://doi.org/10.1029/2020JB021027 959 960 Walter, T. R., and F. Amelung, 2007. Volcanic eruptions following M ≥ 9 megathrust 961 earthquakes: Implications for the Sumatra-Andaman volcanoes. Geology, 35(6), 539–542. 962 https://doi.org/10.1130/G23429A.1 963 964 Wang, D., and J. Mori, 2011. Rupture process of the 2011 off the Pacific coast of Tohoku 965 earthquake (Mw 9.0) as imaged with back-projection of teleseismic P waves. Earth, Planets and 966 Space, 63, 603-607. https://doi.org/10.5047/eps.2011.05.029 967 968 Wang, D., H. Kawakatsu, J. Mori, B. Ali, Z. Ren, and X. Shen, 2016. Back-projection analyses from 969 four regional arrays for rupture over a curved dipping fault: The Mw 7.7 September 24, 2013 970 Pakistan earthquake. Journal of Geophysical Research: Solid Earth, 121(3), 1948–1961. 971 https://doi.org/10.1002/2015JB012168 972 973 Wang, K., and S. L. Bilek, 2014. Fault creep caused by subduction of rough seafloor relief. Tectonophysics, 610, 1-24. https://doi.org/10.1016/j.tecto.2013.11.024 974

976 Wang, K., T. Huang, F. Tilmann, S. M. Peacock, and D. Lange, 2020. Role of serpentinized mantle 977 wedge in affecting megathrust seismogenic behavior in the area of the 2010 M 8.8 Maule 978 earthquake. Geophysical Research Letters, 47, e2020GL090482. https://doi.org/10.1029/2020GL090482 979 980 981 Wang, K., Peng, Z., Liang, S., Luo, J., Zhang, K., & He, C., 2024. Migrating foreshocks driven by a 982 slow slip event before the 2021 MW 6.1 Yangbi, China earthquake. Journal of Geophysical 983 Research: Solid Earth, 129, e2023JB027209. https://doi.org/10.1029/2023JB027209 984 985 Wang, K., Luo, H., He, J. and Carvajal, M., 2025. Soft barrier to megathrust rupture enabled by 986 serpentinized mantle wedge: The Chile subduction zone. Earth and Planetary Science Letters, 987 650, 119115. https://doi.org/10.1016/j.epsl.2024.119115 988 989 Wetzler, N., Lay, T., and Brodsky, E. E., 2023. Global Characteristics of Observable Foreshocks 990 for Large Earthquakes. Seismological Research Letters, 94(5), 2313–2325. 991 https://doi.org/10.1785/0220220397 992 993 Wiemer, S., and M. Wyss, 2002. Mapping spatial variability of the frequency-magnitude 994 distribution of earthquakes. Advances in Geophysics, 45, 259–302. 995 https://doi.org/10.1016/S0065-2687(02)80007-3 996 997 Woessner, J., & Wiemer, S. (2005). Assessing the quality of earthquake catalogues: Estimating 998 the magnitude of completeness and its uncertainty. Bulletin of the Seismological Society of 999 America, 95, 684–698. https://doi.org/10.1785/0120040007 1000 1001 Xu, D., W. Wang, and Z. Ren, 2025. Preliminary slip distribution of the July 29, 2025 Mw 8.8 1002 Kamchatka, Russia earthquake. Earthquake Research Advances, 100427. 1003 https://doi.org/10.1016/j.egrea.2025.100427 1004

1005	Yang, H., L. Zhu, and R. Chu, 2009. Fault-plane determination of the 18 April 2008 Mount
1006	Carmel, Illinois, earthquake by detecting and relocating aftershocks. Bulletin of the
1007	Seismological Society of America, 99(6), 3413–3420. https://doi.org/10.1785/0120090038
1008	
1009	Yagi, Y., Y. Fukahata, R. Okuwaki, T. Takagawa, and S. Toda, 2025. Breaking the cycle: Short
1010	recurrence and overshoot of an M9-class Kamchatka earthquake.
1011	https://doi.org/10.31223/X5475Z
1012	
1013	Yu, C., Z. Li, N. T. Penna, and P. Crippa, 2018. Generic atmospheric correction model for
1014	interferometric synthetic aperture radar observations. Journal of Geophysical Research: Solid
1015	Earth, 123(10), 9202–9222. https://doi.org/10.1029/2017JB015305
1016	
1017	Zhan, Z., D. V. Helmberger, and D. Li, 2014. Imaging subducted slab structure beneath the Sea
1018	of Okhotsk with teleseismic waveforms. Physics of the Earth and Planetary Interiors, 232, 30–
1019	35. https://doi.org/10.1016/j.pepi.2014.03.008
1020	
1021	Zhou, Y., C. Ren, A. Ghosh, H. Meng, L. Fang, H. Yue, et al., 2022. Seismological characterization
1022	of the 2021 Yangbi foreshock-mainshock sequence, Yunnan, China: More than a triggered
1023	cascade. Journal of Geophysical Research: Solid Earth, 127, e2022JB024534.
1024	https://doi.org/10.1029/2022JB024534
1025	
1026	Ziv, A., 2003. Foreshocks, aftershocks, and remote triggering in quasi-static fault models.
1027	Journal of Geophysical Research, 108(B10), 2498. https://doi.org/10.1029/2002JB002318